

NASA Contractor Report 189658

1N-02

113998

P.102

**NAVIER-STOKES COMPUTATIONS OF A
VISCOUS OPTIMIZED WAVERIDER**

Naruhisa Takashima

**UNIVERSITY OF MARYLAND
College Park, Maryland**

**Grant NAG1-1192
June 1992**

(AD-A252649) MODELING FAST
MODULATION EFFECTS IN CESIUM ATOMIC
CLOCKS (Aerospace Corp.) 13 p

N92-30412

Unclass

H2/35 0113252



National Aeronautics and
Space Administration

Langley Research Center
Hampton, Virginia 23665-5225

Abstract

Title of Thesis: Navier-Stokes Computations of a Viscous Optimized Waverider

Name of degree candidate: Naruhisa Takashima

Degree and Year: Master of Science, 1992

Thesis directed by: Dr. Mark J. Lewis
Assistant Professor
Department of Aerospace Engineering

The performance of a Mach 6 viscous optimized waverider was calculated using the three-dimensional Navier-Stokes equations. The Mach 6 viscous optimized waverider was generated using MAXWARP, a waverider generating code developed at the University of Maryland. The numerical calculations were done using CFL3D, an implicit upwind-biased finite volume algorithm developed at NASA-Langley. The results were used for several purposes: validation of the existing waverider generation code, calculation of the on- and off-design performance of a waverider, and assessment of the validity of the use of waverider geometry as a forebody for an engine/airframe integrated design. Good agreement was found between the calculated performance by MAXWARP and results from the Mach 6 Navier-Stokes calculation. Off-design performance of the Mach 6 optimized waverider were calculated for Mach numbers of 4 and 8. The performance at these Mach numbers compared well with the performance of the viscous optimized waveriders specifically designed for these Mach numbers. Contours of different flow parameters in the cross flow plane were examined for the three calculations. The results indicate that the flow gradients are relatively small within the captured flow, and the variation itself is well behaved; thus, making the waverider configuration a promising choice for an engine/airframe design, especially for a cruise type application.

Acknowledgments

I would like to thank my advisor, Mark J. Lewis, for his enthusiasm and support which made this work possible.

Also, I would like to acknowledge the following people for their contributions to this thesis: Dave Miller at the NASA Langley Research Center for providing CFL3D; Sherry Krist and James Thomas at the NASA Langley Research Center for their answers to my questions regarding the code; Jim Randolph and JPL for providing the Cray time which was absolutely necessary for the completion of this work; and the members of the hypersonic group at the University of Maryland, Mary Kae O'Neill in particular, for their moral and technical support.

Lastly, I would like to thank my parents for making it all possible.

Table of Contents

List of Tables	v
List of Figures	vi
List of Symbols	x
1 Introduction	1
1.1 Concept of Waveriders	3
1.2 Generation of Waveriders	4
1.3 Optimization of Waveriders	7
1.4 Present Work	8
2 MAXWARP	10
3 Governing Equations	13
3.1 Nondimensionalization of the Governing Equations	14
3.2 Transformation of the Governing Equations	14
3.3 Thin-Layer Navier-Stokes Equations	16
4 Numerical Algorithm	18
4.1 Spatial Discretization	18
4.1.1 Godunov Method	18
4.1.2 Roe's Flux Difference Splitting	20
4.2 Time Integration	24
4.3 Turbulence Model	27

5	Grid Generation	29
5.1	Elliptic Grid Generation	29
5.2	Grid Spacing	35
5.3	Grid Adaptation	36
6	Results	42
6.1	Configuration	42
6.2	Solution Methodology	43
6.3	Euler Calculation	44
6.4	Navier-Stokes Calculations	45
7	Conclusions and Recommendations	82
7.1	Conclusions	82
7.2	Recommendations	83
	Appendices	84
A	Leading Edge Coordinates	84
	Bibliography	87

List of Tables

6.1	Inviscid force coefficients and L/D for Mach 6 calculation.	45
6.2	Force coefficients and L/D for Mach 6 calculation.	46
6.3	The inviscid, viscous, and the total force coefficients for Mach 6 calculation.	46
6.4	Force coefficients and L/D at on and off-design conditions.	51
A.1	Leading edge coordinates for Mach 6 viscous optimized waverider	85
A.2	Leading edge coordinates for Mach 6 viscous optimized waverider (continued)	86

List of Figures

1.1	Engine/Airframe Integrated Vehicle.	2
1.2	Caret wing.	5
1.3	Conical waverider.	5
1.4	General shock waverider ¹²	6
1.5	Mach Number vs. L/D of Various Configurations ¹⁵	8
2.1	Waverider Generation.	12
5.1	Elliptic grid generation.	34
5.2	Three-dimensional grid for Mach 6 waverider.	39
5.3	Details of the leading edge for the inviscid grid and the viscous grid.	40
5.4	Non-adaptive grid and adaptive grid for Mach 6 inviscid calculation.	41
6.1	Rounding the leading edge.	43
6.2	Mach 6 viscous optimized waverider.	51
6.3	Comparison of MAXWARP results and CFL3D Euler results for Mach 6 calculation: Pressure contour at exit flow plane.	52
6.4	Comparison of MAXWARP results and CFL3D Euler results for Mach 6 calculation: Surface pressure distribution at exit flow plane and the outline of the cross-section.	53
6.5	Surface pressure variation in the streamwise direction from CFL3D results for Mach 6 calculation	54
6.6	Comparison of MAXWARP results and CFL3D results for Mach 6 calculation: Pressure contour at cross-section located at 60 % of the chord.	55

6.7	Comparison of MAXWARP Results and CFL3D Results for Mach 6 calculation: Pressure contour at exit flow plane.	56
6.8	Comparison of MAXWARP results and CFL3D results for Mach 6 calculation: Surface pressure distribution at cross-section located at 60 % of the chord and the outline of the cross-section. .	57
6.9	Comparison of MAXWARP results and CFL3D results for Mach 6 calculation: Surface pressure distribution at the exit flow plane and the outline of the cross-section.	58
6.10	Comparison of MAXWARP results for Mach 6 and CFL3D results for Mach 8 calculation: Pressure contour at cross-section located at 60 % of the chord.	59
6.11	Comparison of MAXWARP results for Mach 6 and CFL3D results for Mach 8 calculation: Pressure contour at exit flow plane.	60
6.12	Comparison of MAXWARP results for Mach 6 and CFL3D results for Mach 8 calculation: Surface pressure distribution at cross-section located at 60 % of the chord and the outline of the cross-section.	61
6.13	Comparison of MAXWARP results for Mach 6 and CFL3D results for Mach 8 calculation: Surface pressure distribution at the exit flow plane and the outline of the cross-section.	62
6.14	Comparison of MAXWARP for Mach 6 results and CFL3D results for Mach 4 calculation: Pressure contour at cross-section located at 60 % of the chord.	63
6.15	Comparison of MAXWARP results for Mach 6 and CFL3D results for Mach 4 calculation: Pressure contour at exit flow plane.	64
6.16	Comparison of MAXWARP results for Mach 6 and CFL3D results for Mach 4 calculation: Surface pressure distribution at cross-section located at 60 % of the chord and the outline of the cross-section.	65

6.17 Comparison of MAXWARP results for Mach 6 and CFL3D results for Mach 4 calculation: Surface pressure distribution at the exit flow plane and the outline of the cross-section.	66
6.18 Comparison of MAXWARP results and CFL3D results for Mach 6 calculation: Mass flux contour at cross-section located at 60 % of the chord and the outline of the cross-section.	67
6.19 Comparison of MAXWARP results and CFL3D results for Mach 6 calculation: Mass flux contour at the exit flow plane and the outline of the cross-section.	68
6.20 Comparison of MAXWARP results for Mach 6 and CFL3D results for Mach 8 calculation: Mass flux contour at cross-section located at 60 % of the chord and the outline of the cross-section.	69
6.21 Comparison of MAXWARP results for Mach 6 and CFL3D results for Mach 8 calculation: Mass flux contour at the exit flow plane and the outline of the cross-section.	70
6.22 Comparison of MAXWARP results for Mach 6 and CFL3D results for Mach 4 calculation: Mass flux contour at cross-section located at 60 % of the chord and the outline of the cross-section.	71
6.23 Comparison of MAXWARP results for Mach 6 and CFL3D results for Mach 4 calculation: Mass flux contour at the exit flow plane and the outline of the cross-section.	72
6.24 Comparison of MAXWARP results and CFL3D results for Mach 6 calculation: Side wash angle contour at cross-section located at 60 % of the chord and the outline of the cross-section.	73
6.25 Comparison of MAXWARP results and CFL3D results for Mach 6 calculation: Side wash angle contour at the exit flow plane and the outline of the cross-section.	74
6.26 Comparison of MAXWARP results for Mach 6 and CFL3D results for Mach 8 calculation: Side wash angle contour at cross-section located at 60 % of the chord and the outline of the cross-section.	75

6.27	Comparison of MAXWARP results for Mach 6 and CFL3D results for Mach 8 calculation: Side wash angle contour at the exit flow plane and the outline of the cross-section.	76
6.28	Comparison of MAXWARP results for Mach 6 and CFL3D results for Mach 4 calculation: Side wash angle contour at cross-section located at 60 % of the chord and the outline of the cross-section.	77
6.29	Comparison of MAXWARP results for Mach 6 and CFL3D results for Mach 4 calculation: side wash angle at the exit flow plane and the outline of the cross-section.	78
6.30	Inviscid and viscous force contribution to the total lift coefficient.	79
6.31	Inviscid and viscous force contribution to the total drag coefficient.	80
6.32	Comparison between the L/D values calculated by CFL3D for the Mach 6 viscous optimized waverider and the L/D values predicted by MAXWARP for the Mach 4, 6, and 8 viscous optimized waveriders.	81

List of Symbols

a	= speed of sound
c	= Sutherland's constant
c_p	= specific heat at constant pressure
e	= total energy per unit volume
p	= pressure
q	= velocity magnitude
$\dot{q}_x, \dot{q}_y, \dot{q}_z$	= heat transfer in x,y,z direction
r	= leading edge radius
t	= time
u, v, w	= velocity components
x, y, z	= cartesian coordinates in physical domain

A, B, C	= Jacobian of the inviscid flux vectors
C_v	= Jacobian of the viscous flux vector
C_D	= drag coefficient
C_L	= lift coefficient
F, G, H	= inviscid flux vectors
H_v	= viscous flux vectors
J	= Jacobian of the transformation
L	= reference length
L/D	= lift over drag
M	= Mach number
Pr	= Prandtl number
Q	= conserved variables

Re = Reynolds number
 T = pressure
 U, V, W = contravariant velocity components

γ = specific heat ratio
 λ = bulk viscosity coefficient
 μ = molecular viscosity coefficient
 ν = kinematic viscosity coefficient
 ρ = density
 τ = shear stress
 ξ, η, ζ = body-fitted coordinates in computational domain
 $\delta_\xi, \delta_\eta, \delta_\zeta$ = partial differential operator in ξ, η, ζ direction

Subscripts

i, j, k = grid indices
 L, R = left and right state of the Riemann problem
 x, y, z = partial derivative with respect to x, y, z
 ξ, η, ζ = partial derivative with respect to ξ, η, ζ
 ∞ = freestream condition

Superscripts

n = time step indicity
 R = exact solution to the Riemann problem
 $*$ = dimensional quantity
 \wedge = variable in computational domain
 \sim = numerical flux
 $-$ = Roe averaged value

Chapter 1

Introduction

The initiation of various programs in different countries to develop aerospace planes to secure independent access to space and to efficiently place payloads in orbit, has revitalized interest in hypersonic vehicles. In the United States, the initiation of the National Aerospace Plane (NASP) program has renewed research efforts in the development of an air-breathing hypersonic vehicle for various applications. These applications are not only space applications but commercial applications such as long-distance passenger or cargo transport, as well as military applications, such as reconnaissance, strategic airlift, interdiction, surveillance, and strategic bombing. However, many technological as well as system related obstacles have to be overcome before the first successful flight. Based on preliminary research, the NASP program defined several critical technologies which were deemed essential for the design of such a vehicle¹. These include the scramjet engine, advanced material, and design of a fully integrated engine and airframe.

As the flight Mach number increases, the relative size of the propulsive system of the vehicle to the airframe becomes large². Thus, to minimize losses, the propulsive system must be an integral part of the airframe. One such design would have the entire underside of the vehicle become the propulsive system. In this design, the forebody, from the nose to the engine entrance, serves as an engine inlet by precompressing the flow going into the combustor, and the aftbody, from the combustor to the tail of the vehicle, acts as an engine nozzle

by expanding the flow exiting from the combustor as shown in Figure 1.1. Thus, for an engine/airframe integrated vehicle, the shape of the forebody can have significant impact on the performance of the hypersonic vehicle. The shape of the forebody must be such that it can precompress the flow sufficiently so that combustion can take place while maintaining flow uniformity. Furthermore, for cruise type applications, the shape should provide high L/D (lift-over-drag).

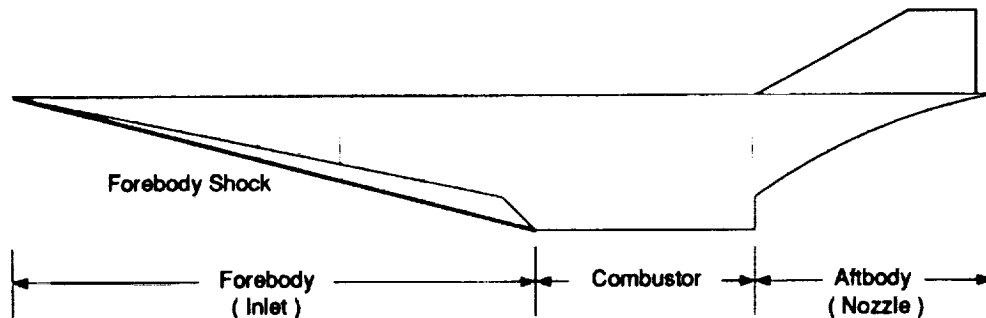


Figure 1.1: Engine/Airframe Integrated Vehicle.

One of the most promising configurations to meet these requirements is an old idea known as the hypersonic waverider. The advantages of the waverider configuration over other configurations are that waveriders generate high L/D and produce a flow field which has no cross flow on the under surface of the body when flown at the design condition. However, the concept, which was first introduced in 1959 by Nonweiler³, has generally been overlooked as a shape for a hypersonic lifting vehicle because the predicted performance of early designs did not match the wind tunnel test results. This was due to the fact that early waveriders were created using inviscid solutions and viscous forces were either

never taken into account or added after the design was determined. Thus, when waveriders were tested in the wind tunnels, they either did not reproduce the predicted performance or achieved poor performance in general.

These problems were resolved with the formulation of viscous optimized waveriders⁴. These conically derived waveriders were unique because skin friction was taken into account in the design process. The end result was a new class of waveriders which exhibited L/D values previously thought unobtainable by a hypersonic vehicle. Since the introduction of the first viscous optimized designs, both subsonic and hypersonic wind tunnel tests have been conducted to assess the viability of various waverider-based configurations for an actual hypersonic vehicle^{5, 6}. The initial results from the hypersonic test have indicated that these configurations do perform as well as predicted by the design code.

1.1 Concept of Waveriders

A waverider is a type of supersonic/hypersonic vehicle which, when flying at the design Mach number, has the entire bow shock on the underside of the vehicle emanating from the leading edge of the body. As a result, there is no flow spillage from the lower surface to the upper surface and the vehicle appears to be riding on top of an attached shock wave; hence, the name "waverider." Two unique features separate the waverider configuration from other supersonic/hypersonic vehicle configurations. First, at the design Mach number, high pressure flow produced by the bow shock is contained beneath the lower surface. This containment of high pressure results in a vehicle with higher lift. In general for a given lift coefficient, waveriders have higher lift-over-drag than other vehicle shapes. Second, not only is the high pressure flow fully contained, but the contained flow has no cross flow, and the inviscid thermodynamic properties are known everywhere in the region. Thus, the waverider configuration is ideally suited for an engine integrated airframe.

1.2 Generation of Waveriders

To generate a waverider, two properties must be first defined: a generating flowfield and either a leading edge curve or a trailing edge curve of a waverider. Given a known generating flowfield and a leading edge curve, the lower surface of a waverider is constructed by tracing the streamsurface from the bow shock downstream to a desired location. Similarly, starting from the trailing edge, the lower surface is formed by tracing the streamlines forward until they intersect the bow shock⁷. Although Bowcutt et al.⁴ used an expansion surface to increase the vehicle's L/D , the upper surface is ordinarily constructed by tracing the freestream surface from the leading edge.

When Nonweiler first introduced the concept of waveriders, better known then as "caret wings" because of their resultant cross-sectional shape, he used a planar oblique shock wave as a generating flowfield as shown in Figure 1.2.

Since then different flowfields including three-dimensional flows have been used to generate waverider shapes. Work was done during the 1960's in Britain, using supersonic flow past cones, to generate a class of "conical-flow" waveriders as shown in Figure 1.3. Later, Rasmussen et al.^{8, 9}, Cole and Zien¹⁰, and Kim et al.¹¹ derived waveriders from circular and elliptic cones, and axisymmetric flow using small disturbance theory. Most recently, Sobieczky et al.¹² constructed waveriders from given shock wave geometries using the method of characteristics as shown in Figure 1.4

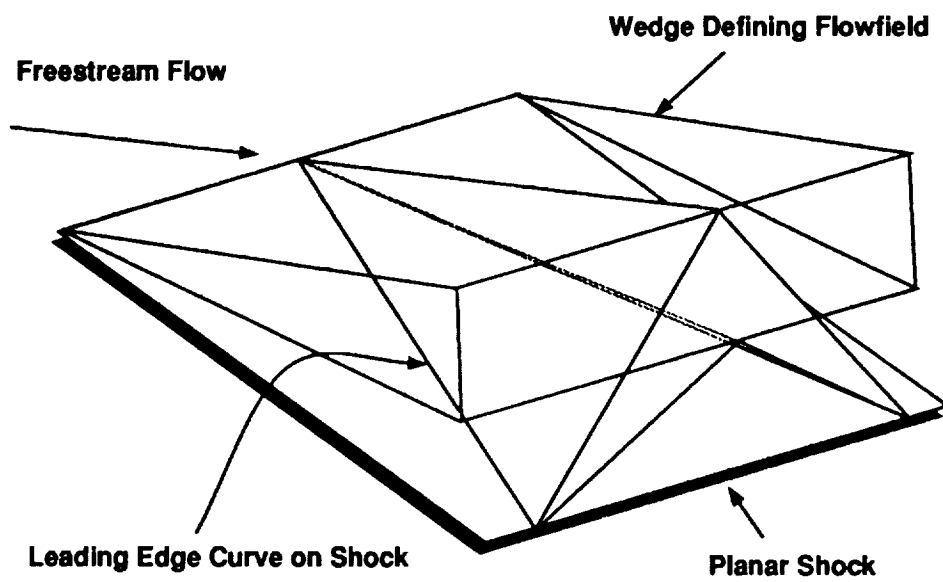


Figure 1.2: Caret wing.

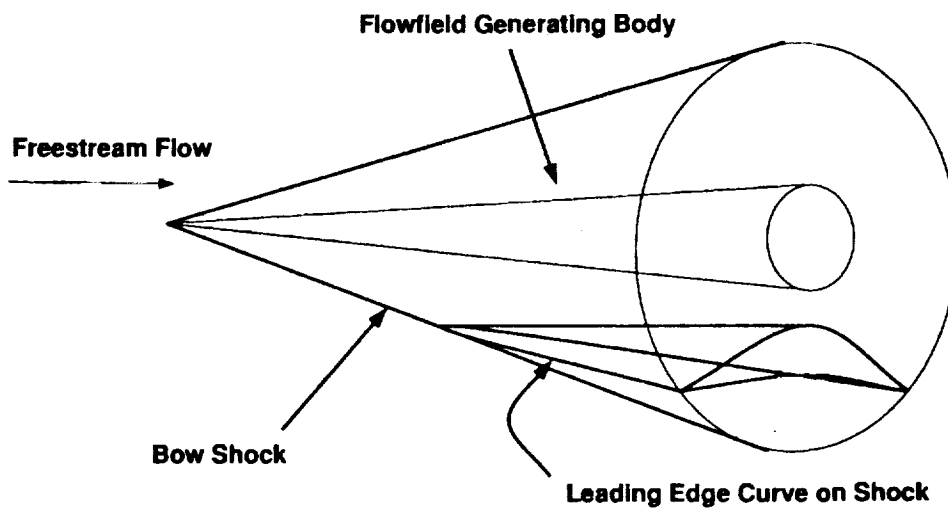


Figure 1.3: Conical waverider.

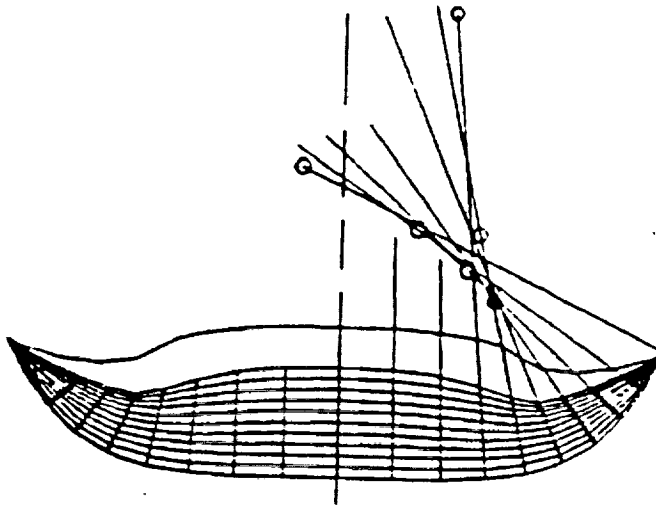
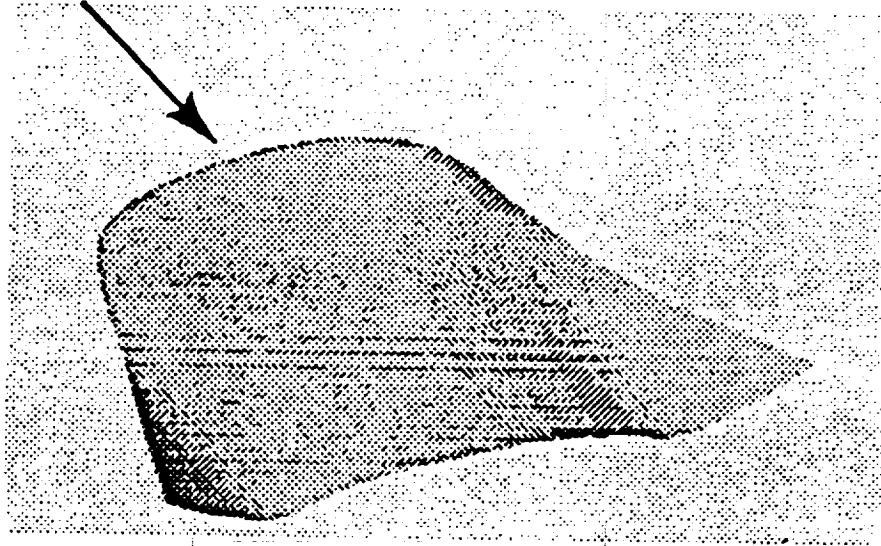


Figure 1.4: General shock waverider¹².

1.3 Optimization of Waveriders

Due to the inverse nature of the method by which waveriders are generated, i.e., the flowfield produced by the waverider at the design condition is known a priori, the waverider lends itself well to various optimization processes. This advantage was first pursued by Rasmussen et al.^{8, 9}, Cole and Zien¹⁰, and Kim et al.¹¹. These authors used small disturbance theory to calculate the surface pressure distribution on a generated vehicle and optimize the shape using the calculus of variations. The concept of "optimized waveriders" was enhanced further by the series of work done at the University of Maryland where the waverider shapes were generated computationally, and the viscous effects were included in the optimization process. The first such work was done by Bowcutt et al.⁴ who solved the integral boundary layer equation along the streamline to calculate the skin friction. The configuration of the vehicle was then optimized for lift-over-drag (L/D) by the simplex method of Nelder and Mead¹³. These waveriders, which were optimized with viscous effects, gave birth to a new class of waveriders coined as "viscous optimized waveriders." The viscous optimized waveriders were unique because they were the first realistic hypersonic configuration to break the " L/D barrier" proposed by Kuchemann¹⁴ as shown in Figure 1.5.

The work on viscous optimized waveriders was continued at the University of Maryland by Corda et al.¹⁵ who used power-law bodies for the generating flowfield in search of a better generating flowfield. Later, McLaughlin¹⁶ used chemically reacting cone-flow for the generating flowfield. Recently, Vanmol¹⁷ optimized the shape for L/D while using the aerodynamic heating as one of the constraint functions, and Chang¹⁸ included viscous interaction effects when calculating the aerodynamic forces. Currently, O'Neill et al.⁷ are optimizing waverider shapes for scramjet engine integration.

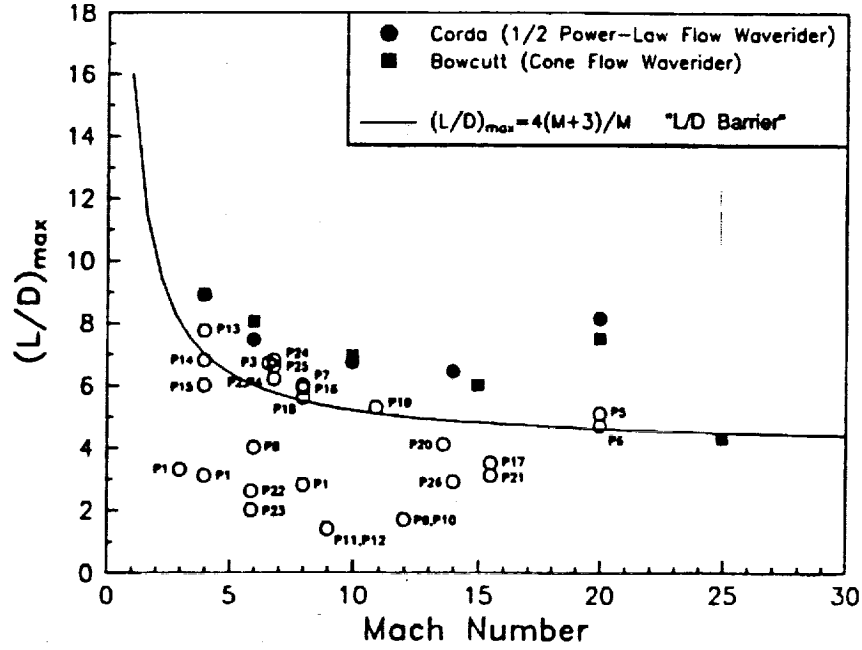


Figure 1.5: Mach Number vs. L/D of Various Configurations¹⁵.

1.4 Present Work

Although the test results confirm the validity of the waverider concept, many more questions must be answered before the waverider geometry is considered as a practical shape for a hypersonic lifting body. These questions include the off-design performance and the effects of leading edge roundness. Since waveriders are point design vehicles, i.e., the the vehicle shape is formed for a given design condition, the performance of the vehicle at on-design conditions is well understood; however, little is known about the off-design performance of viscous optimized waveriders. Furthermore, to maintain an acceptable level of aerodynamic heating, the leading edge of an actual vehicle must be rounded. But the effects of the rounding of the leading edge on the loss of flow containment and subsequent loss of performance is not known. This work is motivated by our interest in the answers to these questions.

In this work the on-design and off-design performance of a Mach 6 viscous optimized waverider are calculated by solving the three-dimensional Navier-

Stokes equations for Mach numbers of 4, 6, and 8. The optimized shape was modified by rounding the leading edge to a radius of 1 cm to study the effect of leading edge roundness. Note that the leading edge radius is small compared to the overall vehicle length of 60m. The results from the Mach 6 calculation are used to validate the existing waverider generation code: MAXWARP. Also, contours of various flow parameters are examined at different cross flow planes to determine the effectiveness of the waverider shape as a forebody design. This work represents the first Navier-Stokes computations of a viscous optimized waverider at off-design Mach numbers.

Chapter 2

MAXWARP

The waverider configuration used for the present study was generated using MAXWARP (Maryland Axisymmetric Waverider Program) computer code¹⁵. MAXWARP is a waverider design code which outputs an optimized waverider geometry generated from either a conical or power-law body flowfield. As mentioned in the previous chapter, the lower surface of the waverider is constructed by tracing the leading edge curve along the bow shock downstream, and the upper surface is defined by the freestream surface as shown for a conical waverider in Figure 2.1.

The surface pressure for the waverider is calculated from the Taylor-Maccoll equation if conical flow is used as a generating flowfield, or from the solutions obtained by solving the Euler equations via a space marching method if the power-law body flowfield is used as a generating flow field. The base pressure of the vehicle is taken to be the freestream pressure value. The skin friction is calculated using the reference temperature method. This method allows approximation for both laminar and turbulent boundary layer. The code allows for fully turbulent flow, fully laminar, and a combination of the two. For the mixed flow, the boundary transition is predicted using a correlation obtained from experimental data.

The shape of the waverider is optimized, either for maximum L/D for a cruise vehicle, or minimum drag for an accelerator, by varying the shape of

the leading edge curve. The optimization process uses the simplex method of Nelder and Mead¹³, and several geometric constraints are imposed for internal volume considerations. Note that the waverider generated by MAXWARP is only optimized for a given generating flowfield; hence, to obtain a true optimum shape for given freestream conditions and wall temperature, a comparison must be made between results for several different generating flowfields.

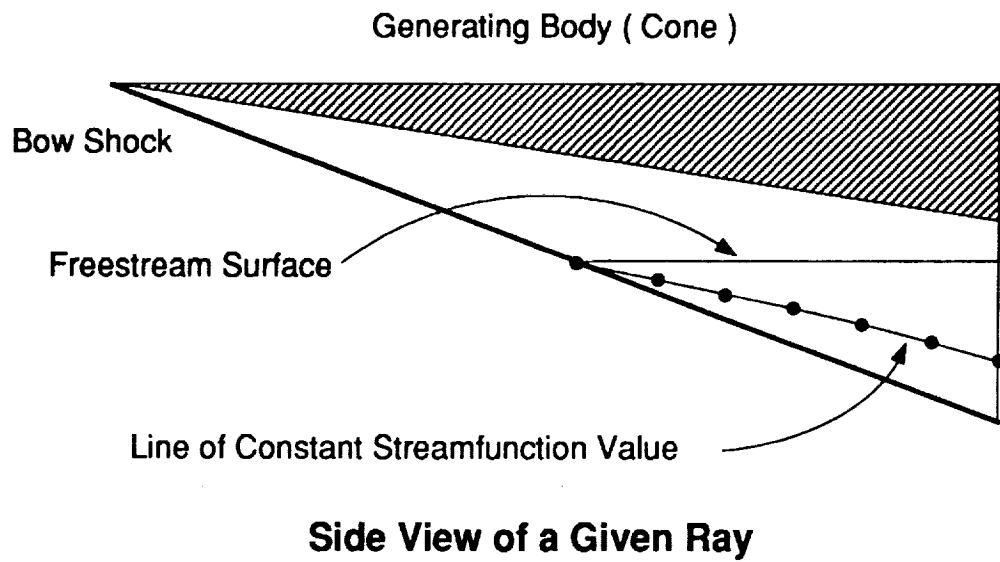
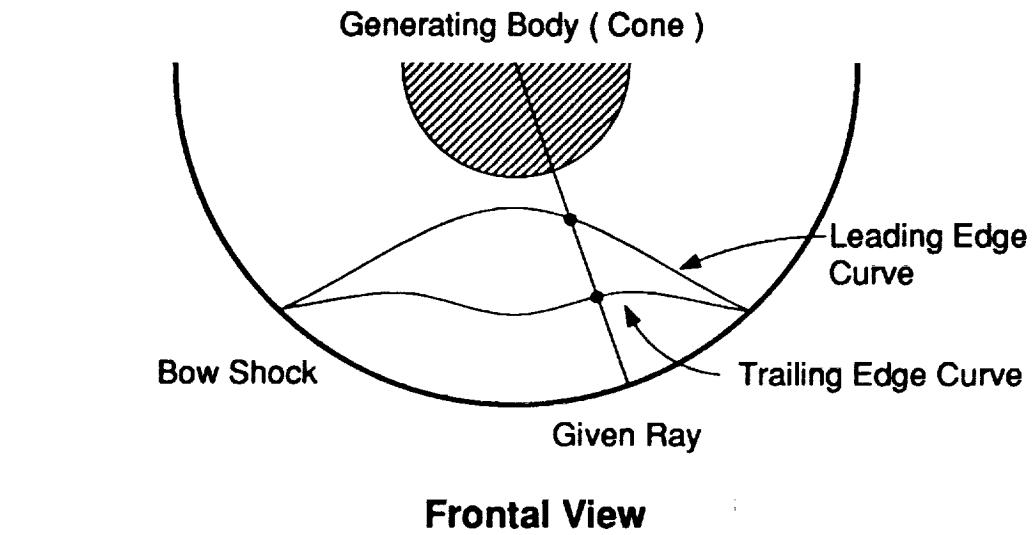


Figure 2.1: Waverider Generation.

Chapter 3

Governing Equations

The computations for the present study were done using CFL3D^{20, 21} provided by NASA Langley Research Center. The governing equations for motion of fluids solved by this code are based on the unsteady, three-dimensional Navier-Stokes equations. Written in a strong conservation form, they are

1. Continuity:

$$\frac{\partial \rho^*}{\partial t^*} + \frac{\partial \rho^* u^*}{\partial x^*} + \frac{\partial \rho^* v^*}{\partial y^*} + \frac{\partial \rho^* w^*}{\partial z^*} = 0 \quad (3.1)$$

2. X-momentum:

$$\frac{\partial \rho^* u^*}{\partial t^*} + \frac{\partial \rho^* u^{*2} + p^*}{\partial x^*} + \frac{\partial \rho^* u^* v^*}{\partial y^*} + \frac{\partial \rho^* u^* w^*}{\partial z^*} = \frac{\partial \tau_{xx}^*}{\partial x^*} + \frac{\partial \tau_{xy}^*}{\partial y^*} + \frac{\partial \tau_{xz}^*}{\partial z^*} \quad (3.2)$$

3. Y-momentum:

$$\frac{\partial \rho^* v^*}{\partial t^*} + \frac{\partial \rho^* u^* v^*}{\partial x^*} + \frac{\partial \rho^* v^{*2} + p^*}{\partial y^*} + \frac{\partial \rho^* v^* w^*}{\partial z^*} = \frac{\partial \tau_{xy}^*}{\partial x^*} + \frac{\partial \tau_{yy}^*}{\partial y^*} + \frac{\partial \tau_{yz}^*}{\partial z^*} \quad (3.3)$$

4. Z-momentum:

$$\frac{\partial \rho^* w^*}{\partial t^*} + \frac{\partial \rho^* u^* w^*}{\partial x^*} + \frac{\partial \rho^* v^* w^*}{\partial y^*} + \frac{\partial \rho^* w^{*2} + p^*}{\partial z^*} = \frac{\partial \tau_{xz}^*}{\partial x^*} + \frac{\partial \tau_{yz}^*}{\partial y^*} + \frac{\partial \tau_{zz}^*}{\partial z^*} \quad (3.4)$$

5. Energy:

$$\begin{aligned} & \frac{\partial e^*}{\partial t^*} + \frac{\partial (e^* + p^*) u^*}{\partial x^*} + \frac{\partial (e^* + p^*) v^*}{\partial y^*} + \frac{\partial (e^* + p^*) w^*}{\partial z^*} = \\ & + \frac{\partial (u^* \tau_{xx}^* + v^* \tau_{xy}^* + w^* \tau_{xz}^* - \dot{q}_x^*)}{\partial x^*} + \frac{\partial (u^* \tau_{xy}^* + v^* \tau_{yy}^* + w^* \tau_{yz}^* - \dot{q}_y^*)}{\partial y^*} + \frac{\partial (u^* \tau_{xz}^* + v^* \tau_{yz}^* + w^* \tau_{zz}^* - \dot{q}_z^*)}{\partial z^*} \end{aligned} \quad (3.5)$$

3.1 Nondimensionalization of the Governing Equations

To obtain dynamic similarity and energetic similarity from geometrically similar situations and to improve the efficiency of the numerical algorithm, the dimensional variables in Equations 3.1-3.5 are nondimensionalized. Among many choices available, the following nondimensional variables are used in CFL3D:

$$\begin{aligned} x &= \frac{x^*}{L^*} & y &= \frac{y^*}{L^*} & z &= \frac{z^*}{L^*} & u &= \frac{u^*}{a_\infty^*} & v &= \frac{v^*}{a_\infty^*} & w &= \frac{w^*}{a_\infty^*} \\ \rho &= \frac{\rho^*}{\rho_\infty^*} & p &= \frac{p^*}{\rho_\infty^* a_\infty^{*2}} & e &= \frac{e^*}{\rho_\infty^* a_\infty^{*2}} \end{aligned} \quad (3.6)$$

The nondimensional shear stresses, in indicial notation, are then given by

$$\tau_{x_i, x_j} = \frac{M_\infty}{Re_\infty} \left[\mu \left(\frac{\partial u_i}{\partial x_j} + \frac{\partial u_j}{\partial x_i} \right) + \lambda \frac{\partial u_i}{\partial x_j} \delta_{ij} \right] \quad (3.7)$$

Similarly, nondimensional heat transfer is given by

$$\dot{q}_{x_i} = - \left[\frac{M_\infty \mu}{Re_\infty Pr(\gamma - 1)} \right] \frac{\partial a^2}{\partial x_i} \quad (3.8)$$

The molecular viscosity in Equations 3.7 and 3.8 is calculated using the Sutherland's Law,

$$\mu = T^{\frac{3}{2}} \frac{1 + c/T_\infty^*}{T + c/T_\infty^*} \quad (3.9)$$

where c is the Sutherland's constant, $c = 198.6^\circ R = 110.4 K$ and Stokes' hypothesis $\lambda = -\frac{2}{3}\mu$ is used for bulk viscosity. The nondimensional parameters are

$$\text{Prandtl number : } Pr = \frac{\mu^* c_p^*}{k^*} = 0.72 \quad (3.10)$$

$$\text{Freestream Reynolds number : } Re_\infty = \frac{\rho_\infty^* q_\infty^* L^*}{\mu_\infty^*} \quad (3.11)$$

$$\text{Freestream Mach number: } M_\infty = \frac{q_\infty^*}{a_\infty^*} \quad (3.12)$$

3.2 Transformation of the Governing Equations

The accuracy and the efficiency of the numerical scheme can be greatly enhanced by transforming the curvilinear physical space into rectangular computational space. For the present study, the unsteady three-dimensional Navier-Stokes equations are transformed from the (x, y, z) Cartesian coordinate system

to a (ξ, η, ζ) body-fitted coordinate system, where the ξ -direction is in the stream-wise direction, the η -direction is in the circumferential direction in the cross-flow plane, and the ζ -direction is in the normal direction from the body. The transformation allows for the simplification of the boundary conditions, and the reduction of overall grid points by clustering the grid in regions where the flow variables experience high gradients and distributing them sparsely in regions of low gradients. The transformation of the equations from Cartesian coordinates to generalized coordinates was done using the following relations,

$$\xi = \xi(x, y, z) \quad (3.13)$$

$$\eta = \eta(x, y, z) \quad (3.14)$$

$$\zeta = \zeta(x, y, z) \quad (3.15)$$

Then using the chain-rule, the transformation metrics can be defined as

$$\xi_x = J(y_\eta z_\zeta - y_\zeta z_\eta) \quad (3.16)$$

$$\eta_x = J(y_\zeta z_\xi - y_\xi z_\zeta) \quad (3.17)$$

$$\zeta_x = J(y_\xi z_\eta - y_\eta z_\xi) \quad (3.18)$$

$$\xi_y = J(x_\zeta z_\eta - x_\eta z_\zeta) \quad (3.19)$$

$$\eta_y = J(x_\xi z_\zeta - x_\zeta z_\xi) \quad (3.20)$$

$$\zeta_y = J(x_\eta z_\xi - x_\xi z_\eta) \quad (3.21)$$

$$\xi_z = J(x_\eta y_\zeta - x_\zeta y_\eta) \quad (3.22)$$

$$\eta_z = J(x_\zeta y_\xi - x_\xi y_\zeta) \quad (3.23)$$

$$\zeta_z = J(x_\xi y_\eta - x_\eta y_\xi) \quad (3.24)$$

where J is the Jacobian of the steady transformation between the Cartesian coordinates (x, y, z) and the generalized coordinates (ξ, η, ζ) given by

$$J = \frac{\partial(\xi, \eta, \zeta)}{\partial(x, y, z)} = \frac{1}{x_\xi(y_\eta z_\zeta - y_\zeta z_\eta) - y_\xi(x_\eta z_\zeta - x_\zeta z_\eta) + z_\xi(x_\eta y_\zeta - x_\zeta y_\eta)} \quad (3.25)$$

3.3 Thin-Layer Navier-Stokes Equations

Since the dominant viscous effects at high Reynolds number arise from viscous diffusion normal to the body and the flowfield is expected to have minimal separation, the thin-layer approximation is employed. The thin-layer approximation neglects all the viscous stresses in the direction parallel to the body surface, which are the ξ and η directions; furthermore, any mixed derivatives are neglected. Then the governing equation used in the present study written in vector form is given by

$$\frac{\partial \hat{Q}}{\partial t} + \frac{\partial \hat{F}}{\partial \xi} + \frac{\partial \hat{G}}{\partial \eta} + \frac{\partial(\hat{H} - \hat{H}_v)}{\partial \zeta} = 0 \quad (3.26)$$

where, \hat{Q} represents the conserved variables,

$$\hat{Q} = \frac{Q}{J} = \frac{1}{J} \begin{bmatrix} \rho \\ \rho u \\ \rho v \\ \rho w \\ e \end{bmatrix} \quad (3.27)$$

\hat{F} , \hat{G} , and \hat{H} represent the inviscid fluxes,

$$\hat{F} = \frac{1}{J} \begin{bmatrix} \rho U \\ \rho U u + \xi_x p \\ \rho U v + \xi_y p \\ \rho U w + \xi_z p \\ (e + p)U \end{bmatrix} \quad (3.28)$$

$$\hat{G} = \frac{1}{J} \begin{bmatrix} \rho V \\ \rho V u + \eta_x p \\ \rho V v + \eta_y p \\ \rho V w + \eta_z p \\ (e + p)V \end{bmatrix} \quad (3.29)$$

$$\hat{H} = \begin{bmatrix} \rho W \\ \rho W u + \zeta_x p \\ \rho W v + \zeta_y p \\ \rho W w + \zeta_z p \\ (e + p)W \end{bmatrix} \quad (3.30)$$

U , V , and W are the contravariant velocity components, which represent velocity components perpendicular to constant planes of ξ , η , and ζ , respectively, and are defined as

$$U = \xi_x u + \xi_y v + \xi_z w \quad (3.31)$$

$$V = \eta_x u + \eta_y v + \eta_z w \quad (3.32)$$

$$W = \zeta_x u + \zeta_y v + \zeta_z w \quad (3.33)$$

The pressure is related to the flow variables by the equation of state for an ideal gas,

$$p = (\gamma - 1) \left[e - \frac{\rho q^2}{2} \right] \quad (3.34)$$

and q^2 is the sum of the squares of the velocities,

$$q^2 = u^2 + v^2 + w^2 \quad (3.35)$$

The viscous flux \hat{H}_ν is given by

$$\hat{H}_\nu = \frac{M_\infty \mu}{Re_\infty J} = \begin{bmatrix} 0 \\ \phi_1 u_\zeta + \zeta_x \phi_2 \\ \phi_1 v_\zeta + \zeta_y \phi_2 \\ \phi_1 w_\zeta + \zeta_z \phi_2 \\ \phi_1 \left[\left(\frac{q^2}{2} \right) + \frac{(a)_\zeta^2}{Pr(\gamma-1)} \right]_\zeta + W \phi_2 \end{bmatrix} \quad (3.36)$$

where

$$\phi_1 = \zeta_x^2 + \zeta_y^2 + \zeta_z^2 \quad (3.37)$$

$$\phi_2 = \frac{(\zeta_x u_\zeta + \zeta_y v_\zeta + \zeta_z w_\zeta)}{3} \quad (3.38)$$

Chapter 4

Numerical Algorithm

CFL3D uses a semi-discrete finite volume method to solve for the governing equations. The steady state solution is obtained using a 3-factor implicit time advancement algorithm. The inviscid flux vectors are upwind differenced using Roe's flux-difference-splitting scheme²² and the viscous flux vector is centrally differenced. The algorithm is second-order accurate in space.

4.1 Spatial Discretization

The semi-discrete finite volume form of the governing equation is given by

$$\begin{aligned} \left(\frac{\partial \bar{Q}}{\partial t}\right)_{i,j,k} + (\bar{F}_{i+\frac{1}{2},j,k} - \bar{F}_{i-\frac{1}{2},j,k}) \\ + (\bar{G}_{i,j+\frac{1}{2},k} - \bar{G}_{i,j-\frac{1}{2},k}) + ((\bar{H} - \bar{H}_\nu)_{i+\frac{1}{2},j,k} - (\bar{H} - \bar{H}_\nu)_{i-\frac{1}{2},j,k}) = 0 \end{aligned} \quad (4.1)$$

where the spatial derivatives are written conservatively as a flux balance across each cell and for convenience the cell size is taken to be unity. In Equation 4.1, subscript (i,j,k) refers to the cell-center location (ξ_i, η_j, ζ_k) , and, for example in the ξ -direction, $i + \frac{1}{2}$ corresponds to the cell interface location $(\xi_{i+\frac{1}{2}}, \eta_j, \zeta_k)$. The inviscid interface fluxes in equation 4.1, \bar{F} , \bar{G} , and \bar{H} are determined by the use of Roe's flux differencing splitting technique which incorporates Roe's approximate Riemann problem solver. The viscous flux \bar{H}_ν is centrally differenced.

4.1.1 Godunov Method

Roe's flux difference splitting method is based on a method originally developed by Godunov²³. In the Godunov method, the conserved variables are

considered piecewise constant within each mesh cell at a given time level, and evolution of the flow to the next time step is based upon the exact solution to the local Riemann problem defined by the conditions across each cell interface. The new constant values for each cell are taken to be the average value of the conserved variable across the cell, thus making this method a finite volume method. The exact relationship for the averaged state is obtained by integrating the conservation equation. For example, integrating the one-dimensional conservation law equation,

$$\frac{\partial Q}{\partial t} + \frac{\partial F}{\partial x} = 0 \quad (4.2)$$

over the domain x to $x + \Delta x$ gives

$$\frac{d}{dt} \int_x^{x+\Delta x} Q(x, t) dx = F(x, t) - F(x + \Delta x, t) \quad (4.3)$$

If the equation is further integrated in time, from $t = n \Delta t$ to $t = (n + 1) \Delta t$, the exact relation is given by,

$$\int_x^{x+\Delta x} Q^{n+1}(x, t) dx - \int_x^{x+\Delta x} Q^n(x, t) dx = -\Delta t [f(Q(x + \Delta x)) - f(Q(x))] \quad (4.4)$$

where f is the time averaged inviscid flux between $t = n \Delta t$ and $t = (n + 1) \Delta t$. If we define the average state variable across the cell x to $x + \Delta x$ as

$$\bar{Q}_i = \frac{1}{\Delta x} \int_{i-\frac{1}{2}}^{i+\frac{1}{2}} Q(x, t) dx \quad (4.5)$$

the exact relation becomes

$$\bar{Q}_i^{n+1} - \bar{Q}_i^n = -\frac{\Delta t}{\Delta x} [f(Q_{i+\frac{1}{2}}) - f(Q_{i-\frac{1}{2}})] \quad (4.6)$$

The equation equates the variation of the cell-averaged conserved variables across time level Δt resulting from the balance of the time-averaged fluxes at the cell interfaces. It is interesting to note that the conservation equation 4.6 has the same form as the general three-point explicit difference scheme in the conservation form,

$$Q_i^{n+1} - Q_i^n = -\frac{\Delta t}{\Delta x} [\bar{F}(Q_{i+\frac{1}{2}}) - \bar{F}(Q_{i-\frac{1}{2}})] \quad (4.7)$$

Hence, the numerical flux of the scheme is considered to be the approximation to the time-averaged physical flux and the mesh point value is the cell-averaged

value. In Godunov's method the numerical flux or the time-averaged flux is obtained from the exact solution to the Riemann problem across each cell interface. Consider $Q^R(x/t, Q_L, Q_R)$ as the exact solution to the Riemann problem defined by the initial conditions,

$$Q = Q_L \quad x < 0 \quad (4.8)$$

$$Q = Q_R \quad x > 0 \quad (4.9)$$

along a ray x/t . The approximation of the time-averaged flux across cell boundaries or the numerical fluxes, $\bar{F}(Q_{i+\frac{1}{2}})$, $\bar{F}(Q_{i-\frac{1}{2}})$, for the Godunov scheme can be calculated from the exact solution to the Riemann problem at each cell boundary, i.e.,

$$\bar{F}(Q_{i-\frac{1}{2}}) = F(Q^R(0, Q_{i-1}, Q_i)) \quad (4.10)$$

$$\bar{F}(Q_{i+\frac{1}{2}}) = F(Q^R(0, Q_i, Q_{i+1})) \quad (4.11)$$

Substituting the above equations into the general conservation equation gives

$$Q_i^{n+1} = Q_i^n - \frac{\Delta t}{\Delta x} [F(Q^R(0, Q_i, Q_{i+1})) - F(Q^R(0, Q_{i-1}, Q_i))] \quad (4.12)$$

4.1.2 Roe's Flux Difference Splitting

In Roe's Flux Difference Splitting Method the numerical flux is the interface flux calculated from the approximate Riemann problem solver of Roe's. The incorporation of an approximate Riemann problem solver is based on the idea that, since the original Godunov scheme relates only an approximation of the exact solution, one might be satisfied with approximate solutions to the Riemann problem if the non-linear behavior of the solution is retained. Roe suggests approximate solutions which are exact solutions to an approximate problem given by

$$Q_t + \bar{A} Q_x = 0 \quad (4.13)$$

The matrix \bar{A} is a constant Jacobian matrix constructed from some average state \bar{Q} which is based on the left and right states, Q_L and Q_R . Roe required that the matrix must satisfy the following properties:

- (1) $F(Q_R) - F(Q_L) = \bar{A}(Q_R, Q_L)(Q_R - Q_L)$
- (2) If $Q = Q_L = Q_R$ then, $\bar{A}(Q_L, Q_R) = A(Q) = \partial F / \partial Q$.
- (3) The eigenvectors of $\bar{A}(Q_L, Q_R)$ are linearly independent.
- (4) It constitutes a linear mapping from the vector space Q to the vector space F

The average states that satisfy these properties are given by

$$\bar{u} = \frac{u_L + Du_R}{1 + D} \quad (4.14)$$

$$\bar{H} = \frac{H_L + DH_R}{1 + D} \quad (4.15)$$

$$\bar{a}^2 = (\gamma - 1)[\bar{H} - \frac{1}{2}\bar{u}^2] \quad (4.16)$$

where

$$D = \sqrt{\frac{\rho_R}{\rho_L}} \quad (4.17)$$

Hence the averaged Jacobian matrix \bar{A} becomes

$$\bar{A} = \begin{bmatrix} 0 & 1 & 0 \\ -(2 - \kappa)u^2 & (2 - \kappa)\bar{u}^2 & \kappa \\ (\frac{\kappa\bar{u}^2}{2} - \bar{H})\bar{u} & \bar{H} - \kappa\bar{u}^2 & (1 + \kappa)\bar{u} \end{bmatrix} \quad (4.18)$$

where $\kappa = (\gamma - 1)$ for perfect gas. The interface flux, i.e., the numerical flux for the scheme, is calculated using

$$\tilde{F}_{i+\frac{1}{2}} = \frac{1}{2}[F(Q_R) + F(Q_L) - \bar{R}|\bar{\Lambda}|\bar{R}^{-1}(Q_R - Q_L)]_{i+\frac{1}{2}} \quad (4.19)$$

where \bar{R} and \bar{R}^{-1} are the right-eigenvector matrix of \bar{A} and its inverse, respectively, and $|\bar{\Lambda}|$ is the diagonal matrix consisting of the absolute values of the eigenvalues of matrix \bar{A} , i.e.,

$$|\bar{\Lambda}| = \begin{bmatrix} |\bar{u} - \bar{a}| & 0 & 0 \\ 0 & |\bar{u}| & 0 \\ 0 & 0 & |\bar{u} + \bar{a}| \end{bmatrix} \quad (4.20)$$

The dissipation term contribution to the interface flux in a three-dimensional generalized curvilinear coordinate system in the ξ direction is given by

$$\begin{aligned}
 |\bar{A}|(Q_R - Q_L) &= |\bar{A}| \Delta Q \\
 &= \begin{bmatrix} a_4 \\ \bar{u}a_4 + k_x a_5 + a_6 \\ \bar{v}a_4 + k_y a_5 + a_7 \\ \bar{w}a_4 + k_z a_5 + a_8 \\ \bar{H}a_4 + \bar{u}a_5 + \bar{u}a_6 + \bar{v}a_7 + \bar{w}a_8 - (\frac{\bar{a}^2 \gamma}{2} - 1)a_1 \end{bmatrix} \quad (4.21)
 \end{aligned}$$

where

$$a_1 = \left| \frac{\nabla \xi}{J} \right| |\bar{u}| \left(\Delta \rho - \frac{\Delta p}{\bar{a}^2} \right) \quad (4.22)$$

$$a_2 = \frac{1}{2\bar{a}^2} \left| \frac{\nabla \xi}{J} \right| |\bar{u} + c| (\Delta p + \bar{\rho} \bar{a} \Delta \bar{u}) \quad (4.23)$$

$$a_3 = \frac{1}{2\bar{a}^2} \left| \frac{\nabla \xi}{J} \right| |\bar{u} - c| (\Delta p + \bar{\rho} \bar{a} \Delta \bar{u}) \quad (4.24)$$

$$a_4 = a_1 + a_2 + a_3 \quad (4.25)$$

$$a_5 = \bar{a}(a_2 - a_3) \quad (4.26)$$

$$a_6 = \left| \frac{\nabla \xi}{J} \right| |\bar{u}| (\rho \Delta u - k_x \bar{\rho} \Delta \bar{u}) \quad (4.27)$$

$$a_7 = \left| \frac{\nabla \xi}{J} \right| |\bar{u}| (\rho \Delta v - k_y \bar{\rho} \Delta \bar{u}) \quad (4.28)$$

$$a_8 = \left| \frac{\nabla \xi}{J} \right| |\bar{u}| (\rho \Delta w - k_z \bar{\rho} \Delta \bar{u}) \quad (4.29)$$

The $\bar{\cdot}$ superscript denotes the Roe averaged states given by

$$\bar{\rho} = \sqrt{\rho_L \rho_R} \quad (4.30)$$

$$\bar{u} = \frac{u_L + u_R D}{1 + D} \quad (4.31)$$

$$\bar{v} = \frac{v_L + v_R D}{1 + D} \quad (4.32)$$

$$\bar{w} = \frac{w_L + w_R D}{1 + D} \quad (4.33)$$

$$\bar{H} = \frac{H_L + H_R D}{1 + D} \quad (4.34)$$

$$\bar{\alpha}^2 = (\gamma - 1) \left[\bar{H} - \frac{(\bar{u}^2 + \bar{v}^2 + \bar{w}^2)}{2} \right] \quad (4.35)$$

where D is given by equation 4.17. $\left| \frac{\nabla \xi}{J} \right|$ is the magnitude of the directed area of the cell interface in the ξ direction and

$$(k_x, k_y, k_z) = -\frac{(\xi_x, \xi_y, \xi_z)}{|\nabla \xi|} \quad (4.36)$$

are the associated direction cosines. The contravariant velocity normal to the cell interface is denoted

$$\dot{u} = k_x u + k_y v + k_z w \quad (4.37)$$

When $Q_L = Q_i$ and $Q_R = Q_{i+1}$ are used for the interface values, the scheme is only first-order accurate in space due to the averaging across the cell; hence, the MUSCL (Monotonic Upstream Scheme for Conservation Laws) approach is applied to Roe's first order scheme to obtain spatially higher order differencing. The interface conserved variables are constructed from the primitive variables $q \equiv [\rho, u, v, w, p]^T$ which are redefined as

$$(q_L)_{i+\frac{1}{2}} = q_i + \frac{1}{4}[(1 - \kappa)(\Delta \bar{q}_i) + (1 + \kappa)(\nabla \bar{q}_i)] \quad (4.38)$$

$$(q_R)_{i+\frac{1}{2}} = q_{i+1} - \frac{1}{4}[(1 + \kappa)(\Delta \bar{q}_{i+1}) + (1 - \kappa)(\nabla \bar{q}_{i+1})] \quad (4.39)$$

where Δ and ∇ are the forward and backward differencing operators, respectively, which are limited to maintain monotonicity by

$$\Delta \bar{q}_i = \text{minmod}(\Delta q_i, \beta \nabla q_i) \quad (4.40)$$

$$\nabla \bar{q}_i = \text{minmod}(\nabla q_i, \beta \Delta q_i) \quad (4.41)$$

where

$$\text{minmod}(x, y) = \max[0, \min(x \text{ sign}(y), y \text{ sign}(x))] \text{ sign}(x) \quad (4.42)$$

$$\beta = \frac{3 - \kappa}{1 - \kappa} \quad (4.43)$$

$$\Delta q_i = q_i - q_{i-1} \quad (4.44)$$

$$\nabla q_i = q_{i+1} - q_i \quad (4.45)$$

κ was set to be $\frac{1}{3}$, which corresponds to third-order spatial discretization, for all of the computations done for this study.

4.2 Time Integration

Since the steady state solution is sought, the governing equation is integrated implicitly in time to take advantage of local time stepping. The time derivative in the governing equation is approximated by first-order forward differencing resulting in the following equation:

$$\frac{\hat{Q}^{n+1} - \hat{Q}^n}{\Delta t} + \left(\frac{\partial \hat{F}}{\partial \xi} \right)^{n+1} + \left(\frac{\partial \hat{G}}{\partial \eta} \right)^{n+1} + \left(\frac{\partial (\hat{H} - \hat{H}_v)}{\partial \zeta} \right)^{n+1} = 0 \quad (4.46)$$

The flux terms in the above equation are non-linear; therefore, a linearized scheme is applied. For example, using a Taylor series expansion, the flux term in ξ direction is approximated by

$$\hat{F}^{n+1} = \hat{F}^n + \frac{\partial \hat{F}}{\partial t} \Delta t + O(\Delta t)^2 \quad (4.47)$$

Using the chain-rule, $\frac{\partial \hat{F}}{\partial t}$ can be rewritten as

$$\frac{\partial \hat{F}}{\partial t} = \frac{\partial \hat{F}}{\partial Q} \frac{\partial \hat{Q}}{\partial t} \quad (4.48)$$

for time independent grid system. Substituting this equation into Equation 4.47 yields

$$\hat{F}^{n+1} = \hat{F}^n + \frac{\partial \hat{F}}{\partial Q} \frac{\partial \hat{Q}}{\partial t} \Delta t + O(\Delta t)^2 \quad (4.49)$$

Using first-order forward differencing for the temporal terms,

$$\frac{\partial \hat{Q}}{\partial t} = \frac{\hat{Q}^{n+1} - \hat{Q}^n}{\Delta t} + O(\Delta t) = \frac{\Delta \hat{Q}}{\Delta t} + O(\Delta t) \quad (4.50)$$

and using

$$A = \frac{\partial \hat{F}}{\partial \hat{Q}} \quad (4.51)$$

Equation 4.49 becomes

$$\hat{F}^{n+1} = \hat{F}^n + \frac{\partial \hat{F}}{\partial \hat{Q}} \Delta \hat{Q} + O(\Delta t)^2 = \hat{F}^n + A \Delta \hat{Q} + O(\Delta t)^2 \quad (4.52)$$

Similarly, the fluxes $\hat{G}, \hat{H}, \hat{H}_\nu$ are linearized as

$$\hat{G}^{n+1} = \hat{G}^n + \frac{\partial \hat{G}}{\partial \hat{Q}} \Delta \hat{Q} + O(\Delta t)^2 = \hat{G}^n + B \Delta \hat{Q} + O(\Delta t)^2 \quad (4.53)$$

$$\hat{H}^{n+1} = \hat{H}^n + \frac{\partial \hat{H}}{\partial \hat{Q}} \Delta \hat{Q} + O(\Delta t)^2 = \hat{H}^n + C \Delta \hat{Q} + O(\Delta t)^2 \quad (4.54)$$

$$\hat{H}_\nu^{n+1} = \hat{H}_\nu^n + \frac{\partial \hat{H}_\nu}{\partial \hat{Q}} \Delta \hat{Q} + O(\Delta t)^2 = \hat{H}_\nu^n + C_\nu \Delta \hat{Q} + O(\Delta t)^2 \quad (4.55)$$

Substituting Equations 4.52 through 4.55 into Equation 4.46 and rearranging terms yields the delta form of the Euler implicit formula which is given by

$$\begin{aligned} & \left[\frac{I}{J \Delta t} + \delta_\xi A + \delta_\eta B + \delta_\zeta (C - C_\nu) \right]^n \Delta Q \\ &= - \left[\frac{\partial \hat{F}}{\partial \xi} + \frac{\partial \hat{G}}{\partial \eta} + \frac{\partial (\hat{H} - \hat{H}_\nu)}{\partial \zeta} \right]^n = -(RHS)^n \end{aligned} \quad (4.56)$$

where

$$\Delta Q = Q^{n+1} - Q^n \quad (4.57)$$

Note that RHS is evaluated at the known time level. Applying the spatially-split approximation-factorization method, Q at the $n+1$ step is calculated by

$$\left[\frac{I}{J \Delta t} + \delta_\xi A \right]^n \Delta Q^* = -(RHS)^n \quad (4.58)$$

$$\left[\frac{I}{J \Delta t} + \delta_\eta B \right]^n \Delta Q^{**} = \left[\frac{I}{J \Delta t} \right]^n \Delta Q^* \quad (4.59)$$

$$\left[\frac{I}{J \Delta t} + \delta_\zeta (C - C_\nu) \right]^n \Delta Q = \left[\frac{I}{J \Delta t} \right]^n \Delta Q^{**} \quad (4.60)$$

$$Q^{n+1} = Q^n + \Delta Q \quad (4.61)$$

where δ is the difference operator and the subscript denotes the direction. Each of the spatial factors is approximated with a diagonal inversion of the Jacobian matrix. For example in the ξ direction

$$\begin{aligned}
\left[\frac{I}{J\Delta t} + \delta_\xi A\right]^n \Delta Q^* &= \left[\frac{I}{J\Delta t} + \delta_\xi (R\Lambda R^{-1})\right]^n \Delta Q^* \\
&= \left[\frac{I}{J\Delta t} + \delta_\xi (R(\Lambda^+ + \Lambda^-)R^{-1})\right]^n \Delta Q^* \\
&\approx R\left[\frac{I}{J\Delta t} + \delta_\xi^- \Lambda^+ + \delta_\xi^+ \Lambda^-\right]R^{-1} \Delta Q^* \quad (4.62)
\end{aligned}$$

where

$$\Lambda^\pm = \frac{\Lambda \pm |\Lambda|}{2} \quad (4.63)$$

and a first-order backward differencing approximation (δ^-) is used for the positive diagonal matrix (Λ^+), and a first-order forward differencing approximation (δ^+) is used for the negative (Λ^-) diagonal matrix. Then the ξ -sweep of the time integration becomes

$$\left[\frac{I}{J\Delta t} + \delta_\xi^- \Lambda^+ + \delta_\xi^+ \Lambda^-\right](R^{-1} \Delta Q^*) = -R^{-1}(RHS) \quad (4.64)$$

Since the first three elements of the diagonal matrix are the same, only three scalar tridiagonal LU decompositions are required for each sweep. The tridiagonal matrix equation is given by

$$\begin{aligned}
& -\Lambda^+(M_{i-\frac{1}{2}}, Q_{i-1})(R^{-1} \Delta Q^*)_{i-1} \\
& + \left[\frac{I}{J\Delta t} + \Lambda^+(M_{i+\frac{1}{2}}, Q_i) - \Lambda^-(M_{i-\frac{1}{2}}, Q_i)\right](R^{-1} \Delta Q^*)_i \\
& - \Lambda^-(M_{i+\frac{1}{2}}, Q_{i+1})(R^{-1} \Delta Q^*)_{i+1} = -R_i^{-1}(RHS)_i \quad (4.65)
\end{aligned}$$

where, for example, $\Lambda^+(M_{i-\frac{1}{2}}, Q_i)$ denotes that the metric terms M are evaluated at cell interface location $i - \frac{1}{2}$, and the state variables are evaluated at cell-center location i in Λ^+ . The direction cosines of the cell interface orientation contained in the diagonalization matrix R^{-1} are averaged values so that they represent values at cell-centered locations. For the ζ direction, the spectral radius scaling of the viscous Jacobian matrix developed by Coakley²⁴ is used. The ζ spatial

factor is approximated as

$$[\frac{I}{J\Delta t} + \delta_\zeta(C - C_\nu)]^n \Delta Q \approx R[\frac{I}{J\Delta t} + \delta_\zeta^- \Lambda^+ + \delta_\zeta^+ \Lambda^- + \delta_\zeta^2 \nu I] R^{-1} \Delta Q \quad (4.66)$$

where

$$\delta_\zeta^2 f = \frac{f_{i+1} - 2f_i + f_{i-1}}{(\Delta x)^2} \quad (4.67)$$

$$\nu = \frac{\mu_{max}}{\rho} \quad (4.68)$$

and μ_{max} is the largest eigenvalue of C_ν , that is, $\mu_{max} = \max((4/3)\mu, (\gamma/Pr)\mu)$.

4.3 Turbulence Model

The effects of turbulence are accounted for through the concept of eddy viscosity and eddy conductivity. The molecular viscosity μ is replaced by an effective viscosity μ_e and similarly the thermal conductivity k is replaced by an effective thermal conductivity k_e . The effective viscosity is calculated by

$$\mu_e = \mu + \mu_t \quad (4.69)$$

μ_t is the eddy viscosity which is calculated using the algebraic turbulence model of Baldwin and Lomax¹⁹. By using Reynolds analogy, the effective thermal viscosity is calculated by,

$$k_e = k + k_t = \frac{c_p \mu}{Pr} (1 + \frac{Pr}{Pr_t} \frac{\mu_t}{\mu}) \quad (4.70)$$

where Pr_t is the “turbulent” Prandtl number and a value of 0.8 is used.

The turbulence model by Baldwin and Lomax is a zero-equation model where the turbulent boundary layer is divided into two zones: inner region and outer region. The eddy viscosity in the inner region is approximated by

$$\mu_t = \rho l^2 |\omega_z| \quad (4.71)$$

where ω_z is the vorticity defined as

$$\omega_z = \frac{\partial u}{\partial y} - \frac{\partial v}{\partial x} \quad (4.72)$$

The outer region is approximated by

$$\mu_t = \alpha \bar{\rho} C_{cp} F_{wake} F_{Kleb} \quad (4.73)$$

where α and C_{cp} are constants with values of 0.018 and 1.6, respectively, and F_{wake} is

$$F_{wake} = \min \left[y_{max} G_{max}, C_{wake} y_{max} \frac{(\Delta V)}{G_{max}} \right] \quad (4.74)$$

A value of 0.25 is typically taken for C_{wake} and G_{max} is defined as

$$G_{max} = \max \left(\frac{l}{\kappa} |\omega_x| \right) \quad (4.75)$$

where $\kappa \approx 0.4$ is the von Karman constant. The mixing length, l , is determined by

$$l = \kappa (1 - e^{-\frac{y^+}{A^+}}) y \quad (4.76)$$

where standard definition of y^+ is

$$y^+ = y \frac{\sqrt{\tau_w / \rho}}{\nu} \quad (4.77)$$

A^+ is a parameter with a value of 26.0. ΔV denotes the difference between the absolute values of the maximum and minimum values of vorticity within the viscous region. F_{Kleb} is the Klebanoff intermittency factor, given by

$$F_{Kleb} = \left[1 + 5.5 \left(C_{Kleb} \frac{y}{y_{max}} \right)^6 \right]^{-1} \quad (4.78)$$

where $C_{kleb} = 0.3$ and y_{max} is the y location where G_{max} occurs.

Chapter 5

Grid Generation

5.1 Elliptic Grid Generation

To solve the governing equations by means of a finite difference approximation, a set of grid points within the domain of interest, as well as the boundaries of the domain must first be specified. Furthermore, to solve the governing equations given by Equation 4.1 accurately, a grid system with the following properties is desired²⁵:

- (1) A guaranteed one-to-one mapping, which ensures grid lines of same families do not cross each other.
- (2) Smooth variation of grid points.
- (3) Clustering of grid lines near the surface
- (4) Orthogonality of the grid lines near the surface

To satisfy these properties, the grid system used for this study was generated using an elliptic grid generation method developed by Steger and Sorenson²⁵. In this method a system of partial differential equations is solved in a computational domain for the physical grid points as shown in Figure 5.1.

The governing partial differential equations, in the physical domain, are given by

$$\frac{\partial^2 \eta}{\partial y^2} + \frac{\partial^2 \eta}{\partial z^2} = P(\eta, \zeta) \quad (5.1)$$

$$\frac{\partial^2 \zeta}{\partial y^2} + \frac{\partial^2 \zeta}{\partial z^2} = Q(\eta, \zeta) \quad (5.2)$$

where $P(\eta, \zeta)$ and $Q(\eta, \zeta)$ are the forcing functions which ensure grid clustering and orthogonality near the boundaries. Transforming the Equations 5.1 and 5.2 by exchanging the independent and dependent variables, gives

$$\alpha \frac{\partial^2 y}{\partial \eta^2} - 2\beta \frac{\partial^2 y}{\partial \eta \partial \zeta} + \gamma \frac{\partial^2 y}{\partial \zeta^2} = -J^2 \left(P \frac{\partial y}{\partial \eta} + Q \frac{\partial y}{\partial \zeta} \right) \quad (5.3)$$

$$\alpha \frac{\partial^2 z}{\partial \eta^2} - 2\beta \frac{\partial^2 z}{\partial \eta \partial \zeta} + \gamma \frac{\partial^2 z}{\partial \zeta^2} = -J^2 \left(P \frac{\partial z}{\partial \eta} + Q \frac{\partial z}{\partial \zeta} \right) \quad (5.4)$$

where

$$\alpha = \frac{\partial^2 y}{\partial \zeta^2} + \frac{\partial^2 z}{\partial \zeta^2} \quad (5.5)$$

$$\beta = \frac{\partial y}{\partial \eta} \frac{\partial y}{\partial \zeta} + \frac{\partial z}{\partial \eta} \frac{\partial z}{\partial \zeta} \quad (5.6)$$

$$\gamma = \frac{\partial^2 y}{\partial \eta^2} + \frac{\partial^2 z}{\partial \eta^2} \quad (5.7)$$

$$J = \frac{\partial y}{\partial \eta} \frac{\partial z}{\partial \zeta} - \frac{\partial y}{\partial \zeta} \frac{\partial z}{\partial \eta} \quad (5.8)$$

The Equations 5.3 and 5.4 are two independent equations, which are solved in the computational space (η, ζ) for the physical grid coordinates (y, z) . To obtain a grid which is orthogonal and clustered at the surface ($\zeta = \zeta_1$), Steger and Sorenson proposed forcing functions having the form,,

$$P = p(\eta, \zeta_1) e^{-a(\zeta - \zeta_1)} \quad (5.9)$$

$$Q = q(\eta, \zeta_1) e^{-b(\zeta - \zeta_1)} \quad (5.10)$$

where a and b are specified constants. While the governing elliptic equations provide the smooth one-to-one distribution of points, the forcing functions, $p(\eta, \zeta_1)$ and $q(\eta, \zeta_1)$, must be derived to satisfy the other two desirable properties, namely

grid clustering and orthogonality at the inner boundaries. At the inner body, $\zeta = \zeta_1$, Equations 5.3 and 5.4 yield two independent equations for the forcing functions, $p(\eta, \zeta_1)$ and $q(\eta, \zeta_1)$, given by

$$p(\eta, \zeta_1) = \left[\frac{\frac{\partial z}{\partial \zeta} R_1 - \frac{\partial y}{\partial \zeta} R_2}{J} \right]_{\zeta=\zeta_1} \quad (5.11)$$

$$q(\eta, \zeta_1) = \left[\frac{-\frac{\partial z}{\partial \eta} R_1 + \frac{\partial y}{\partial \eta} R_2}{J} \right]_{\zeta=\zeta_1} \quad (5.12)$$

where

$$R_1 = \left[\frac{-(\alpha \frac{\partial^2 y}{\partial \eta^2} - 2\beta \frac{\partial^2 y}{\partial \eta \partial \zeta} + \gamma \frac{\partial^2 y}{\partial \zeta^2})}{J^2} \right]_{\zeta=\zeta_1} \quad (5.13)$$

$$R_2 = \left[\frac{-(\alpha \frac{\partial^2 z}{\partial \eta^2} - 2\beta \frac{\partial^2 z}{\partial \eta \partial \zeta} + \gamma \frac{\partial^2 z}{\partial \zeta^2})}{J^2} \right]_{\zeta=\zeta_1} \quad (5.14)$$

For the above equations, since the boundary values are fixed along $\zeta = \zeta_1$, all the η -derivatives, y_η , z_η , $y_{\eta\eta}$, and $z_{\eta\eta}$ can be calculated using known boundary point values. The first ζ -derivatives are derived so that grid orthogonality and clustering can be maintained at the inner boundary. As shown in Figure 5.1, the spacing between the inner boundary and the first constant ζ line can be described as

$$\Delta s|_{\zeta=\zeta_1} = \left[\sqrt{(\Delta y)^2 + (\Delta z)^2} \right]_{\zeta=\zeta_1} \quad (5.15)$$

In the limit as Δy and Δz go to zero,

$$ds|_{\zeta=\zeta_1} = \left[\sqrt{(dy)^2 + (dz)^2} \right]_{\zeta=\zeta_1} \quad (5.16)$$

Using the chain rule, the equation can be expanded as

$$ds|_{\zeta=\zeta_1} = \left[\sqrt{\left(\frac{\partial y}{\partial \eta} d\eta + \frac{\partial y}{\partial \zeta} d\zeta \right)^2 + \left(\frac{\partial z}{\partial \eta} d\eta + \frac{\partial z}{\partial \zeta} d\zeta \right)^2} \right]_{\zeta=\zeta_1} \quad (5.17)$$

Since η is constant along $\zeta = \zeta_1$, the above relationship can be reduced to

$$ds|_{\zeta=\zeta_1} = \left[\sqrt{\left(\frac{\partial y}{\partial \zeta} d\zeta\right)^2 + \left(\frac{\partial z}{\partial \zeta} d\zeta\right)^2} \right]_{\zeta=\zeta_1} \quad (5.18)$$

which can be rewritten as

$$\left(\frac{ds}{d\zeta}\right)_\zeta|_{\zeta=\zeta_1} = \left[\sqrt{\left(\frac{\partial y}{\partial \zeta}\right)^2 + \left(\frac{\partial z}{\partial \zeta}\right)^2} \right]_{\zeta=\zeta_1} \quad (5.19)$$

To achieve grid orthogonality along the inner boundary, consider the definition of a dot product,

$$[\nabla \eta \cdot \nabla \zeta]_{\zeta=\zeta_1} = [|\nabla \eta| |\nabla \zeta| \cos \theta]_{\zeta=\zeta_1}$$

where $\theta = \pi/2$ gives grid orthogonality. Expanding the equation gives

$$\left[\frac{\partial \eta}{\partial y} \frac{\partial \zeta}{\partial y} + \frac{\partial \eta}{\partial z} \frac{\partial \zeta}{\partial z} \right]_{\zeta=\zeta_1} = \left[\sqrt{\left(\frac{\partial \eta}{\partial y}\right)^2 + \left(\frac{\partial \eta}{\partial z}\right)^2} \sqrt{\left(\frac{\partial \zeta}{\partial y}\right)^2 + \left(\frac{\partial \zeta}{\partial z}\right)^2} \cos \theta \right]_{\zeta=\zeta_1} \quad (5.20)$$

Exchanging the independent and dependent variables gives

$$\left[\frac{\partial y}{\partial \eta} \frac{\partial \zeta}{\partial \eta} + \frac{\partial z}{\partial \eta} \frac{\partial \zeta}{\partial \zeta} \right]_{\zeta=\zeta_1} = - \left[\sqrt{\left(\frac{\partial y}{\partial \zeta}\right)^2 + \left(\frac{\partial z}{\partial \zeta}\right)^2} \sqrt{\left(\frac{\partial y}{\partial \eta}\right)^2 + \left(\frac{\partial z}{\partial \eta}\right)^2} \cos \theta \right]_{\zeta=\zeta_1} \quad (5.21)$$

Combining equations (5.19) and (5.21) produces the first ζ -derivatives,

$$\left(\frac{\partial y}{\partial \zeta}\right)_{\zeta=\zeta_1} = \left[\frac{\frac{ds}{d\zeta} \left(-\frac{\partial y}{\partial \eta} \cos \theta - \frac{\partial z}{\partial \eta} \sin \theta \right)}{\sqrt{\left(\frac{\partial y}{\partial \eta}\right)^2 + \left(\frac{\partial z}{\partial \eta}\right)^2}} \right]_{\zeta=\zeta_1} \quad (5.22)$$

$$\left(\frac{\partial z}{\partial \zeta}\right)_{\zeta=\zeta_1} = \left[\frac{\frac{ds}{d\zeta} \left(-\frac{\partial z}{\partial \eta} \cos \theta + \frac{\partial y}{\partial \eta} \sin \theta \right)}{\sqrt{\left(\frac{\partial y}{\partial \eta}\right)^2 + \left(\frac{\partial z}{\partial \eta}\right)^2}} \right]_{\zeta=\zeta_1} \quad (5.23)$$

The cross derivatives $y_{\eta\zeta}$ and $z_{\eta\zeta}$ can be then calculated by differencing the known derivatives y_ζ and z_ζ with respect to η . Note that all the derivatives

mentioned above are calculated from known boundary point values, so they do not change with iteration levels. Only the derivatives $y_{\zeta\zeta}$ and $z_{\zeta\zeta}$ change with each iteration, which can be calculated by

$$y_{\zeta\zeta}|_{\zeta=\zeta_1} = \frac{-7y|_{\zeta=\zeta_1} + 8y|_{\zeta=\zeta_2} - y|_{\zeta=\zeta_3}}{2(\Delta\zeta)^2} - \frac{3y_{\zeta}|_{\zeta=\zeta_1}}{\Delta\zeta} \quad (5.24)$$

$$z_{\zeta\zeta}|_{\zeta=\zeta_1} = \frac{-7z|_{\zeta=\zeta_1} + 8z|_{\zeta=\zeta_2} - z|_{\zeta=\zeta_3}}{2(\Delta\zeta)^2} - \frac{3z_{\zeta}|_{\zeta=\zeta_1}}{\Delta\zeta} \quad (5.25)$$

With a given initial grid distribution and desired minimum spacing along the inner boundary, Equations 5.3 and 5.4 can be solved using any relaxation scheme for elliptic partial differential equations. One note of caution, the p and q values calculated by Equations 5.11 and 5.12 can be quite large, which in turn can cause instabilities during the initial iterations. Hence, the values of p and q are under-relaxed. The new values of p and q at each iteration are calculated by

$$p^n = p^{n-1} + \text{SIGN} \{ \min [\omega_p | p - p^{n-1} |, p_{lim} \max(|p^{n-1}|, 1)] , p - p^{n-1} \} \quad (5.26)$$

$$q^n = q^{n-1} + \text{SIGN} \{ \min [\omega_q | q - q^{n-1} |, q_{lim} \max(|q^{n-1}|, 1)] , q - q^{n-1} \} \quad (5.27)$$

where superscript $n-1$ denotes the previous iteration values. The function SIGN returns the magnitude of the first argument and the sign of the second argument. p_{lim} is a small constant which is inputted. Furthermore, instabilities can occur if the first-derivatives on the right-hand side of Equations 5.3 and 5.4 are centrally differenced; therefore, the derivatives are approximated using forward or backward differencing, depending on the sign of p and q . For example, if p is positive, the η derivatives are approximated using forward differencing, and if it is negative, backward differencing is used. The ζ derivatives are calculated similarly, depending on the sign of q . For the present study, Line Successive Over-Relaxation was used to solve Equations 5.3 and 5.4, and grid sequencing was used to minimize computational time. The value for ω_p and ω_q was .09, and p_{lim} and q_{lim} varied with the iteration level from 0.1 to 0.5. The exponential constants a and b varied from 0.4 to .8, depending on the axial location where the grid was generated.

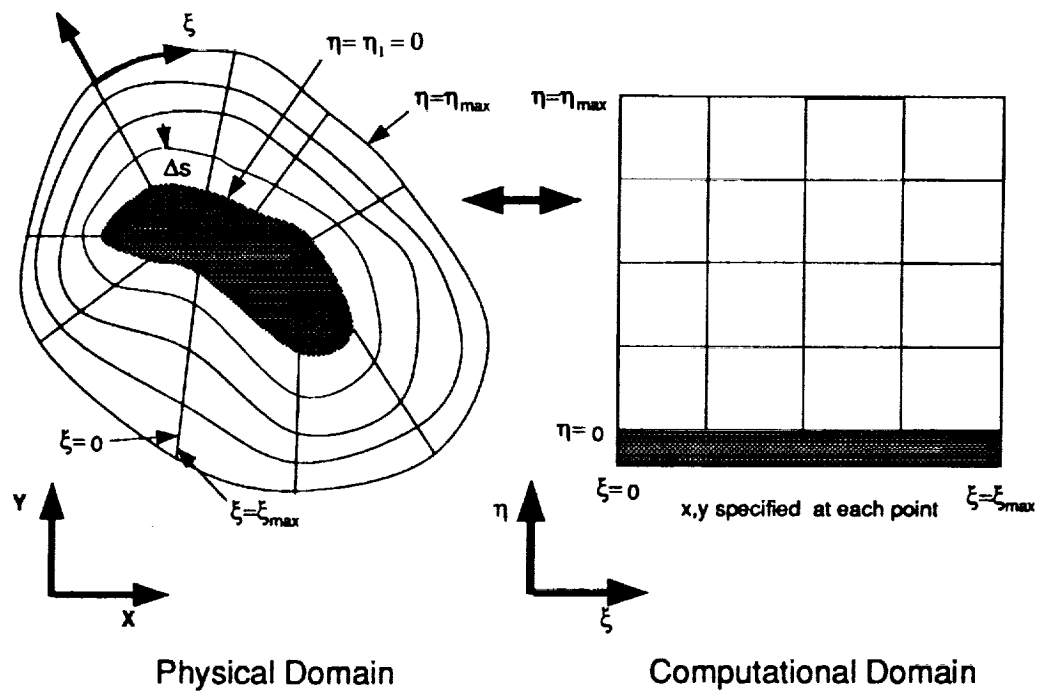


Figure 5.1: Elliptic grid generation.

5.2 Grid Spacing

For the Euler calculation, the grid spacing between the surface and the first constant ζ -line was set to be of the order of 10^{-3} everywhere. For the viscous calculations, to ensure accurate prediction of the skin friction the size of the first grid cell away from the body is more critical than in the inviscid calculations. The general rule of thumb, based on past calculations of this type, is that the grid spacing should be such a size so that the corresponding y^+ values to the center of the first grid cells are of order of one-tenth. y^+ is the standard height parameter used in turbulent flow calculations, given by

$$y^+ = \frac{\Delta y \sqrt{\frac{\tau_w}{\rho}}}{\nu} \quad (5.28)$$

where Δy is the grid size, τ_w is the wall shear stress, ρ is the density, and ν is the coefficient of kinematic viscosity. Thus, the required height of the first grid cell can be calculated by solving the above equation for y^+ . This was done by approximating the wall density, the kinematic viscosity, and the shear stress using the reference temperature method. In this method, the local turbulent skin friction coefficient is given by

$$c_f = \frac{0.0592}{(Re'_x)^{0.2}} \quad (5.29)$$

where

$$Re'_x = \frac{\rho' V_\infty x}{\mu'} \quad (5.30)$$

ρ' and μ' are, the density and viscosity respectively evaluated at the reference temperature, T' , given by

$$T' = T_\infty [1 + 0.032 M_e^2 + 0.58 (\frac{T_w}{T_\infty} - 1)] \quad (5.31)$$

where M_e is the edge Mach number and T_w is the wall temperature. Viscosity is assumed to vary exponentially; hence, μ' is calculated by

$$\frac{\mu'}{\mu} = (\frac{T'}{T_\infty})^\omega \quad (5.32)$$

and ω is set to be 0.75 for the present work. The wall shear stress is calculated by

$$\tau_w = c_f \left(\frac{1}{2} \rho' V_\infty \right) \quad (5.33)$$

For the present study, the edge Mach number was set to be the freestream Mach number instead of local edge Mach number for convenience and a value of $y^+ = 0.2$ was used. The grid spacing calculated using Equation 5.28 was then multiplied by a parameter which varied from the leading edge point to the center-line, having a maximum value at the leading edge point and a minimum value at the center-line to account for the fixed Mach number. Since this is only an approximation, the actual values of y^+ must be checked to ensure the accuracy of the results. For all cases, the actual values of y^+ based on results from the calculation varied from 0.1 to 0.5; thus, satisfying the condition stated previously.

The final three-dimensional grid was obtained by connecting the two-dimensional grid generated for each axial-location, which results in a C-H topology. The grid for the region in front of the nose was constructed by duplicating the grid at the nose and placing it in front of the body. The grid topology for the Mach 6 Euler calculation is shown in Figure 5.2. Figure 5.3 shows the details of the grid near the sharp leading edge for the inviscid calculation and the rounded leading edge for the viscous calculations. Superimposed on the sharp leading edge is the shape of the rounded leading edge.

5.3 Grid Adaptation

To achieve better shock resolution, an adapted grid was used for the inviscid calculation of a sharp leading edge waverider at on-design conditions. The adapted grid was generated using a method developed by Hsu and Lytle²⁶ The idea behind the scheme, known as the arc equidistribution scheme, is to have the grid size inversely proportional to a weight function so that the product of the weight function and the grid size are approximately equal at each grid cell. When the gradient of the flow variables is used to construct the weight

function, the grid will be dense at regions of high gradient thus reducing the discretization error in the region.

$$\Delta S_j w_j = \lambda C_j \quad (5.34)$$

where

$$\Delta S = \sqrt{(x_{j+1} - x_j)^2 + (y_{j+1} - y_j)^2} \quad (5.35)$$

and

$$w_j = 1 + \beta |u_{j+1} - u_j| \quad (5.36)$$

u represents any of the flow variable, as well as, any combinations. β is a constant which controls the sensitivity of adaptation to the flow gradient. Larger value of β will cause the grid to be more dense in the region for given flow gradient. C_j is taken to be

$$C_j = \Delta S_j^o \quad (5.37)$$

where the superscript "o" denotes the arc lengths of the original non-adaptive grid. This allows for the new grid to have a memory of the spacing of the original grid; hence the new grid will be similar to the original grid. Coefficient λ is a constant which is determined so that the total arc length of the new grid is the same as the old arc, i.e.,

$$\sum_j \Delta S_j^o = \sum_j \Delta S_j = \lambda \sum_j \frac{C_j}{w_j} \quad (5.38)$$

From the above equation

$$\lambda = \frac{\sum_j \Delta S_j^o}{\sum_j \frac{C_j}{w_j}} \quad (5.39)$$

After obtaining a flowfield solution from the non-adaptive grid, the grid was clustered in the regions of high pressure gradient in the ζ direction; hence, Equation 5.36 becomes

$$w_k = 1 + \beta |p_{k+1} - p_k| \quad (5.40)$$

with $\beta = 50$. For each constant ζ -line, two sets of cubic-splines with the arc length as the independent variable and x and y as the dependent variables are created.

The new arc length is calculated from Equation 5.34, and to ensure a smooth grid, the new arc lengths are averaged using a four point averaging,

$$S_{j,k} = \frac{1}{4}(S_{j+1,k} + S_{j-1,k} + S_{j,k-1} + S_{j,k+1}) \quad (5.41)$$

The smoothing process, which is in fact a Point Jacobian Method for a Laplace equation, is applied for two or three iterations. Finally, using the new arc length and the cubic-splines, the grid points are redistributed along each constant ζ -line. Figure 5.4 shows the original non-adaptive grid and the adaptive grid at the exit flow plane.

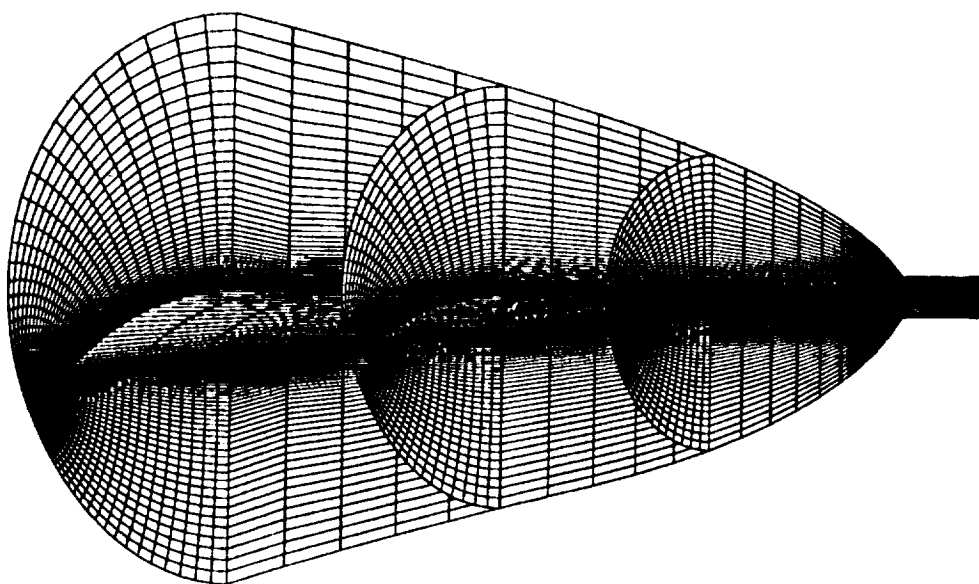
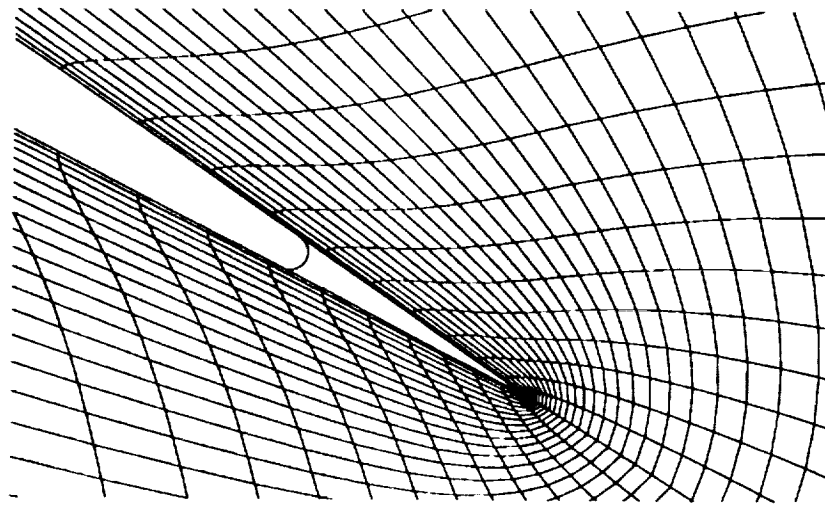
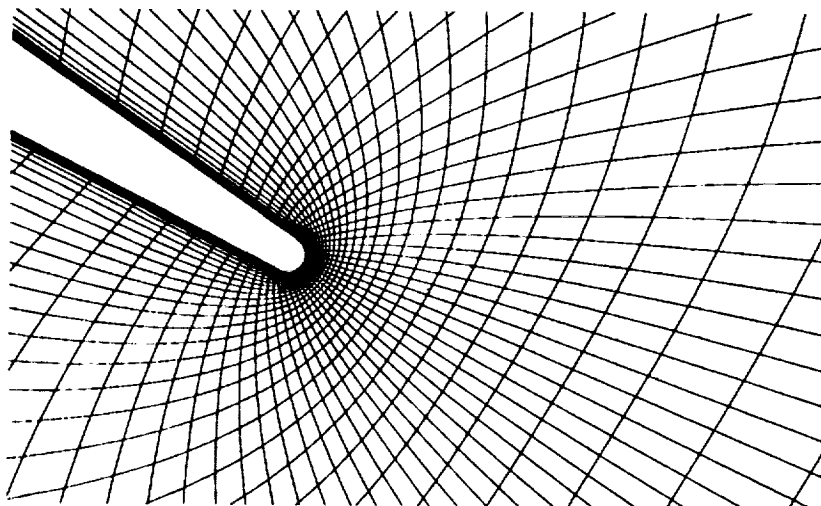


Figure 5.2: Three-dimensional grid for Mach 6 waverider.



Inviscid Grid



Viscous Grid

Figure 5.3: Details of the leading edge for the inviscid grid and the viscous grid.

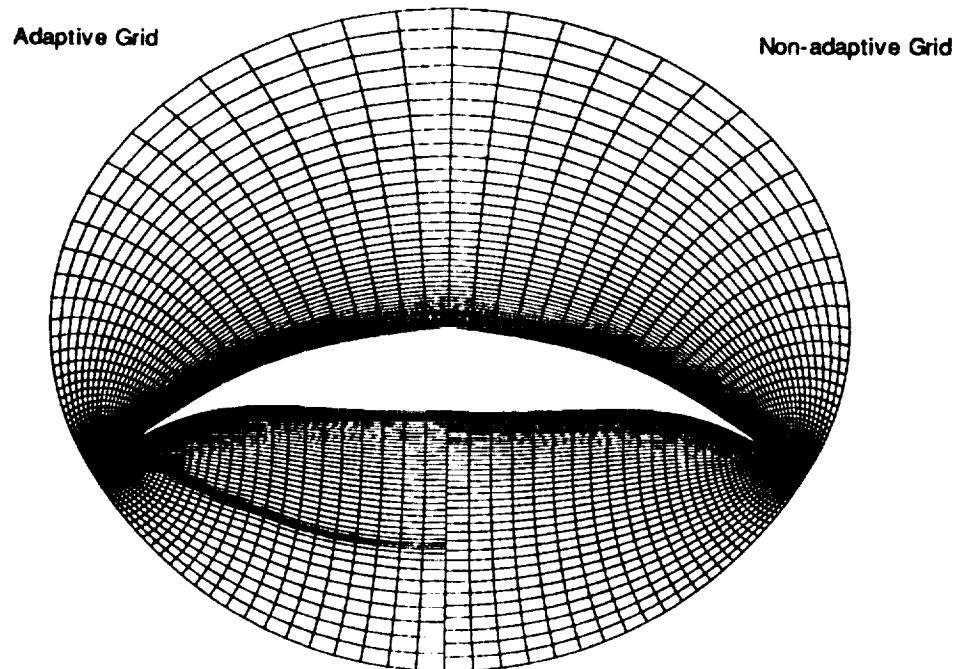


Figure 5.4: Non-adaptive grid and adaptive grid for Mach 6 inviscid calculation.

Chapter 6

Results

6.1 Configuration

The waverider shape used in this study was generated in a flowfield produced by a cone with a semi-apex angle of 7.09 degrees. The design Mach number was Mach 6, and the design static conditions correspond to freestream conditions at an altitude of 30 km. Note that this design condition corresponds to typical hypersonic cruise conditions. The bow shock angle produced by the cone-body at this Mach number is 12 degrees. The leading edge coordinates for this waverider are given in Appendix A. The length of the vehicle was set to be 60 meters, and the surface temperature was set to be a constant value of 1,100 K. The boundary layer was assumed to be fully turbulent everywhere on the vehicle, and the shape was optimized for maximum L/D. This configuration corresponds to the so-called “best optimum” waverider for maximum L/D at the given design condition. The top, front, and perspective view of this waverider are shown in Figure 6.2.

To give realistic meaning to the viscous calculation and to study the effects of leading-edge roundness, the original sharp leading edge was rounded. For the present study the radius of the leading edge was set to be $r = 1$ cm, which corresponds to the minimum radius necessary for active cooling, as explained by Vanmol¹⁷. The leading edge was rounded for each cross-section by moving

inward from the leading edge until the radius of the inscribed circle of a triangle matched the desired leading edge radius. The triangle was constructed at the leading edge using three grid points and everywhere else by extending the line segments defined by the two surface grid points as shown in Figure 6.1.

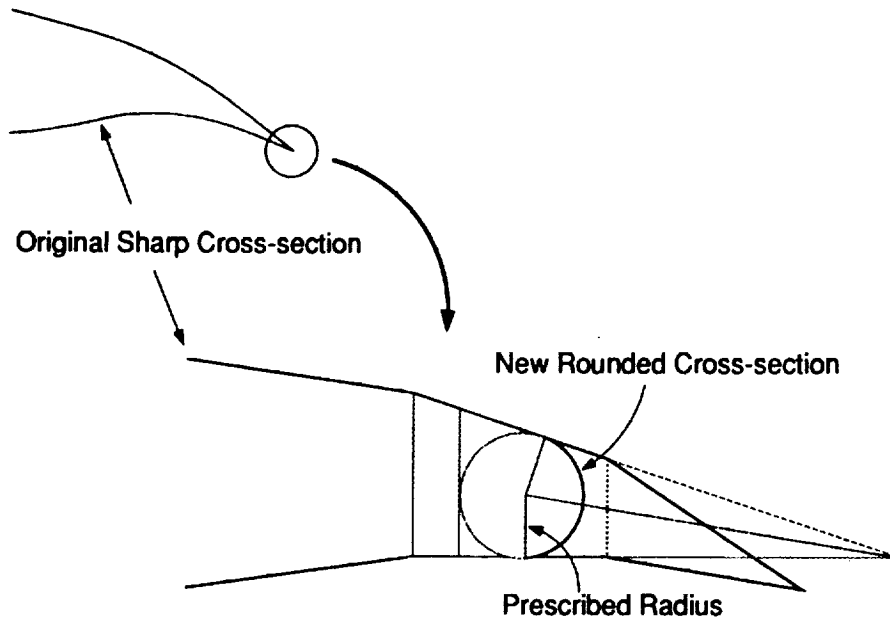


Figure 6.1: Rounding the leading edge.

6.2 Solution Methodology

All computations were run on an waverider, which was optimized for a Mach 6 cruise flight at an altitude of 30 km, as previously stated. The values of freestream static pressure and static temperature were taken to be the design point values of 1185.5 N/m^2 and 231.3 K , respectively. All the cases were run at zero degrees angle of attack, i.e., the upper surface was aligned with the freestream flow. The flow was assumed to be calorically perfect and a specific heat ratio value of 1.4 was used. Inviscid calculations were done for both the rounded leading edge waverider and the original sharp leading edge waverider

at the on-design freestream Mach number of 6. Viscous calculations were done for the rounded leading edge waverider at off-design Mach numbers of 4 and 8, as well as the on-design Mach number. The flow was assumed to be fully turbulent, and the wall temperature was set at the design wall temperature value of 1100 K for Mach 6 and 8 calculations and 725 K for Mach 4 calculation, everywhere on the vehicle.

Second-order extrapolation was used for the exit flow plane boundary condition. A global iteration was performed for all of the calculations until the drag coefficient varied by less than one-tenth of a percent over 100 iterations.

A grid dimension of $21 \times 91 \times 51$, which corresponds to the dimension of the grid in the ξ , η , and ζ directions, respectively, was used for the Mach 6 and 8 calculations. The values of the dimension correspond to the number of grid points in the streamwise direction, circumferential direction, and the radial direction, respectively. For the Mach 4 calculation a $46 \times 91 \times 51$ grid was used. When the computation was originally done for Mach 4 using $26 \times 91 \times 51$ grid, the code produced results with compression waves emanating from the lower surface, which were not present in the higher Mach number calculations. By increasing the number of points in the streamwise direction to 46, the non-physical waves caused by minor surface irregularities were eliminated.

6.3 Euler Calculation

The pressure data from MAXWARP can be taken as an "exact solution" to the inviscid flow field, within the numerical errors associated with the fourth-order Runge-Kutta method and cubic-spline interpolation of the cone-flow. Therefore, the inviscid results from MAXWARP, i.e., the Taylor-Maccoll solution can be used for validation of the Euler results. Figure 6.3 is the pressure contour plot at the exit flow plane. The left portion of the diagram represents the "exact solution," where the pressure was calculated for each grid point using the cone-flow solution from MAXWARP and a cubic-spline interpolation. The right portion of the diagram is constructed from the Euler solution obtained from the computation. Note the excellent agreement in the shock location. The

slight difference in the locations of the pressure contour lines within the shock is primarily due to the finite shock thickness calculated by the Euler solution. Also, the minor differences may be caused by the extrapolation of the cell averaged values which are calculated by the finite volume algorithm. The surface pressure distribution at the exit flow plane is shown in Figure 6.4. Except near the center-line, both solutions are in good agreement. Once again, differences near the center-line are due to the finite shock thickness calculated by the Euler solution. Table 6.3 lists the force coefficients, C_L and C_D , and L/D calculated by MAXWARP and CFL3D. The values predicted from the two codes are in good agreement. For both codes the base drag was calculated using the freestream static pressure value.

	MAXWARP	CFL3D	% Difference
C_L	3.172E-2	3.168E-2	.126
C_D	2.257E-3	2.315E-3	2.57
L/D	14.06	13.68	2.70

Table 6.1: Inviscid force coefficients and L/D for Mach 6 calculation.

6.4 Navier-Stokes Calculations

One of the primary objectives of this study is the validation of the viscous forces predicted by the MAXWARP design code. Since the leading edges of the waverider for the Navier-Stokes calculations were rounded, the bow shock will no longer be attached to the leading edge. Therefore, the pressure and viscous force in the region near the leading edge will be different from the original configuration and a direct comparison between the two results will not be exact; however, since the leading edge radius is significantly smaller than the overall size of the vehicle, the computational results should compare well with the MAXWARP prediction. Table 6.2 shows the direct comparison of the force coefficients and L/D predicted by the two codes, and Table 6.3 shows the contributions of the inviscid and viscous forces to the total force predicted by the

two codes. The performance predicted by the two codes compares very well. The CFL3D calculates lift and drag coefficients that are 1.86% and 6.87%, respectively, higher than the MAXWARP code predictions. The larger increase in drag coefficient is due to the effects of the leading edge roundness on the inviscid flowfield, which can be seen by comparing the inviscid drag coefficients, i.e., the wave drag coefficient in Table 6.3. It is noted that the viscous contribution to the total drag is practically the same for both codes.

	MAXWARP	CFL3D	% Difference
C_L	3.168E-2	3.228E-2	1.86
C_D	4.089E-3	4.391E-3	6.87
L/D	7.74	7.35	5.31

Table 6.2: Force coefficients and L/D for Mach 6 calculation.

Code		Inviscid	Viscous	Total
MAXWARP	C_L	3.172E-2	-.004E-2	3.168E-2
	C_D	2.257E-3	1.832E-3	4.089E-3
CFL3D	C_L	3.237E-2	-.009E-2	3.228E-2
	C_D	2.549E-3	1.842E-3	4.391E-3

Table 6.3: The inviscid, viscous, and the total force coefficients for Mach 6 calculation.

Figure 6.5 show the surface pressure variation in the streamwise direction along the centerline on the top and bottom surface, and the leading edge. Along the leading edge, the pressure monotonically decreases from a maximum value at the nose region to a minimum value at the trailing edge. This variation is analogous to the variation of the sweep angle. On the other hand, the surface pressure monotonically increases along the centerline on the bottom surface, which is consistent with the pressure variation along a streamline in a conical flow. Note that along the centerline on the top surface, the pressure remains essentially constant. Figures 6.6 and 6.7 show the pressure contours at a cross-

section located at 60% of the chord and at the exit flow plane, respectively. Both figures show that, although there is some increase in pressure in the flowfield above the vehicle, the increase is minor and the flow can be said to be essentially contained. The shock is located near where the Taylor-Maccoll equation predicts, and the flow within the shock is still very uniform and varies like the conical-flowfield; however, the values are no longer the same for given locations. This is caused by the displacement of the flow away from the body by the boundary layer, which causes the pressure to be at a higher value than the cone-flow value at a given radial direction away from the surface.

Figures 6.8 and 6.9 show the surface pressure distribution at a cross-section located at 60% of the chord and at the exit flow plane. Both figures show marked increase in pressure at the leading edge compared to the design code solution due to the stagnation flow. Immediately downstream of the leading edge, the flow rapidly expands on both side of the surface and then recompresses to pressures slightly higher than the conical values. The difference gradually decreases towards the center-line and returns to the values of the conical-flow.

Figures 6.10 and 6.11 show the pressure contours at a cross-section located at 60% of the chord and at the exit flow plane, respectively, for the Mach 8 off-design calculation. As expected the shock is pressed closer to the body near the center-line and is about two-thirds of the height of the on-design shock location; also, the bow-shock has less curvature in the cross-flow plane, and the pressure varies almost two-dimensionally. Near the leading edge, the flow variation is qualitatively similar to the on-design flowfield, even though the bow shock shape is no longer circular.

Figures 6.12 and 6.13 show the surface pressure distribution at a cross-section located at 60% of the chord and at the exit flow plane, respectively. Due to the higher jump in pressure across the bow shock, the surface pressure ratio is about 25 % higher than the on-design value. But, the surface pressure still varies similarly to the on-design condition, decreasing towards the leading edge until it is affected by the stagnation flow.

Figures 6.14 and 6.15 show the surface pressure distribution at a cross-section

located at 60% of the chord and at the exit flow plane, respectively, for the Mach 4 off-design calculation. As expected, compared to the on-design Mach number calculation, the shock detachment is pronounced. The overall uniformity of the flowfield within the shock is better than the higher Mach number cases due to a weaker shock, and the variation of the flowfield no longer matches the conical flowfield. Also, compared to the higher Mach number flows, the leading edge has a greater influence on the neighboring flowfield.

Figures 6.16 and 6.17 show the surface pressure distribution at a cross-section located at 60% of the chord and at the exit flow plane. In both figures the variation of surface pressure in the circumferential direction no longer behaves like the higher Mach number cases. On the lower surface the pressure is almost constant across the span except near the leading edge where it increases to the stagnation value.

The static pressure contour plots for different Mach numbers indicate that the maximum percent difference in the pressure within the region where the combustor entrance would be most likely located is approximately 10 %, thus providing initial indications of flow uniformity.

Figures 6.18 -6.23 show the mass flux distributions at the 60% chord plane and the exit plane for the three Mach number calculations. Mass flux distribution is a good measure of inlet performance, since loss in mass flux results in a reduction in thrust, and large gradients in mass flux tend to require complex fueling schedules. Figures 6.18 and 6.19 show the mass flux distributions, at the 60% chord plane and the exit plane, respectively for the design Mach number of 6. As a comparison the mass flux distribution for the inviscid flow is shown on the left hand side of the figures. At each cross-section the effect of the boundary layer is to increase the region of higher mass flux; however, the boundary layer also results in a region of large gradient. Comparing the two cross-section, although there is a slight decrease in the magnitude, the distribution of the mass flux at the 60% chord is more uniform than the distribution at the exit plane.

Figures 6.20-6.21 show the distributions for Mach 8 case. The plots show that compared to Mach 6 results, the gradient of the mass flux is greater, but the

distribution is similar along radial direction away from the body to the shock. Note that the boundary thickness based on mass flux nondimensionalized with respect to freestream conditions is thinner than the Mach 6 boundary layer.

Figures 6.22-6.23 show the mass flux distributions for the Mach 4 case. Neglecting the flow within the boundary layer, the region of uniform mass flux has greatly increased at this lower Mach number. This result tends to indicate that the flow about the body has become more two-dimensional, as the freestream Mach number was decreased.

Another good measure of forebody design is the amount of side wash angle at the entrance of the combustor. The increase in side wash angle contributes to reduction in thrust due to loss of momentum in the flight direction and shock generation on the side walls of the combustor. Figures 6.24- 6.29 show the side wash angle distributions at the 60% chord plane and the exit plane for the three cases. Once again, for comparison purposes, the side wash angle distribution for the Mach 6 inviscid flow is shown on the left hand side of the figures.

Figures 6.24 and 6.25 show the side wash angle distributions for the Mach 6 case. Since the generating flow is conical, the side wash angle is equal to the angle between the line of symmetry and the ray emanating from the vertex of the generating cone, as seen in the left hand side of the figures. At each cross-section, the side wash angle within the region of the inviscid shock layer matches closely to the inviscid solution; thus, if a modular scramjet design were to be used, the effects of side wash can be reduced. For example, if six modules with a total width of a third of the span of the vehicle were used, the flow angularity experienced by each module would be roughly less than ± 1.5 degrees. Note that at both cross sections the side wash angle is larger than the corresponding ray angle, which may be the influence of the rounded leading edge.

Figures 6.26 and 6.27 show the side wash angle distributions for the Mach 8 case. The side wash angle distributions are similar to the Mach 6 distribution in that the side wash angle in the inviscid shock layer increases with the ray angle and the angularity within the boundary layer is greater than the angle of the ray; however, the similarity degrades near the leading edge. Note that for

this Mach number the magnitude of the side wash angle remains slightly less than the corresponding ray angle.

Figures 6.28 and 6.29 show the side wash angle distributions for the Mach 4 case. The side wash angle distributions for the Mach 4 results are in stark contrast to previous flow distribution plots, where the flow parameters exhibited little variation. In fact, the side wash angle gradient in the span wise direction for the Mach 4 case is greater than the gradients for the higher Mach number cases. The higher gradient is the result of the larger shock separation from the leading edge.

The lift and drag coefficients and the L/D values for the on-design as well as the two off-design cases are tabulated in Table 6.4. Figure 6.30 and 6.31 show the break down of the lift and drag coefficients. The dominant lift, as expected, is generated by the inviscid pressure on the lower surface for all the ranges of Mach number. The effects of leakage do increase with Mach number, but the overall effects on the lift are minimal. For the drag coefficient, skin friction contributes approximately half the total drag, with the contribution increasing at off-design conditions. As expected the drag coefficient on the upper surface, which can be taken essentially as the skin friction coefficient, decreases with increasing Mach number.

Figure 6.32 compares the L/D values of the Mach 6 waverider used in the present investigation with the viscous optimized waveriders at different Mach numbers. The L/D values for the viscous optimized waveriders were calculated by MAXWARP using the same conditions as the CFL3D calculations. As expected, the difference in performance do increases at off-design conditions; however, overall, the off-design performance of the Mach 6 waverider compares well with the performance of waveriders optimized for the off-design conditions.

	C_L	C_D	L/D
Mach 4	4.354E-2	5.679E-3	7.66
Mach 6	3.228E-2	4.391E-3	7.35
Mach 8	2.520E-2	3.726E-3	6.76

Table 6.4: Force coefficients and L/D at on and off-design conditions.

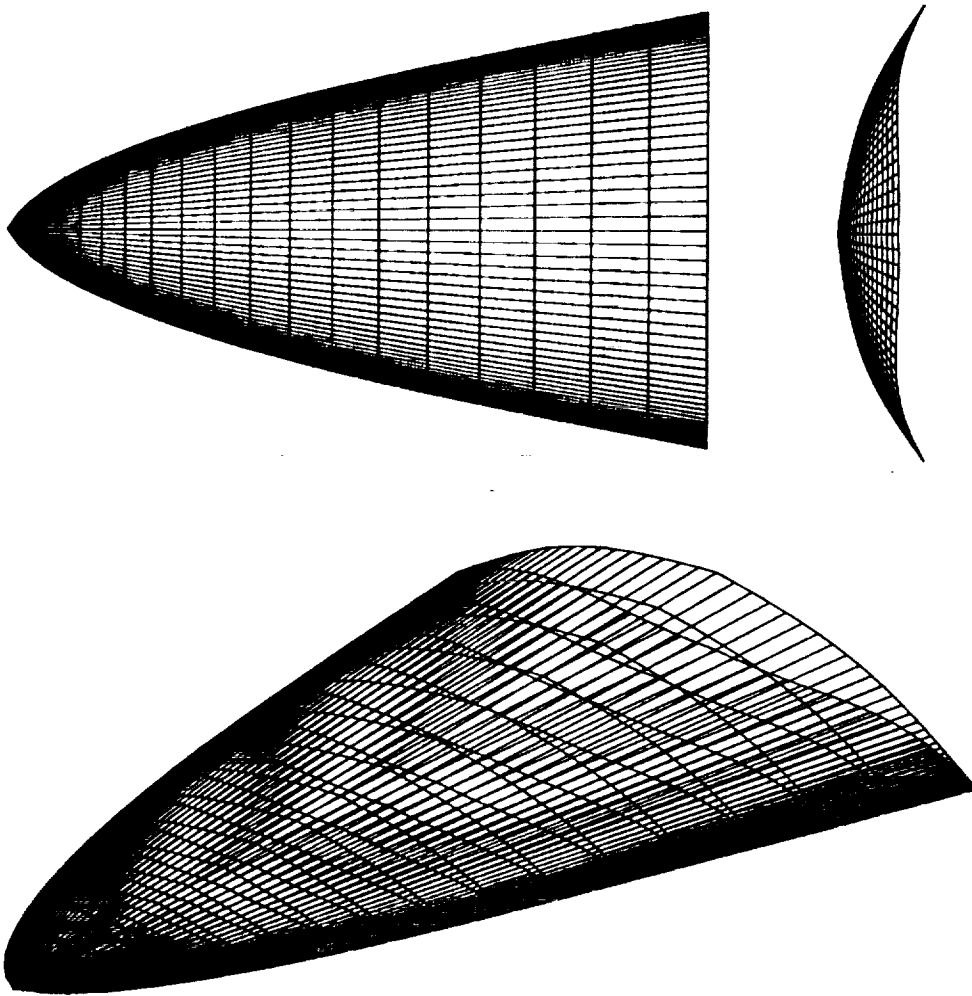


Figure 6.2: Mach 6 viscous optimized waverider.

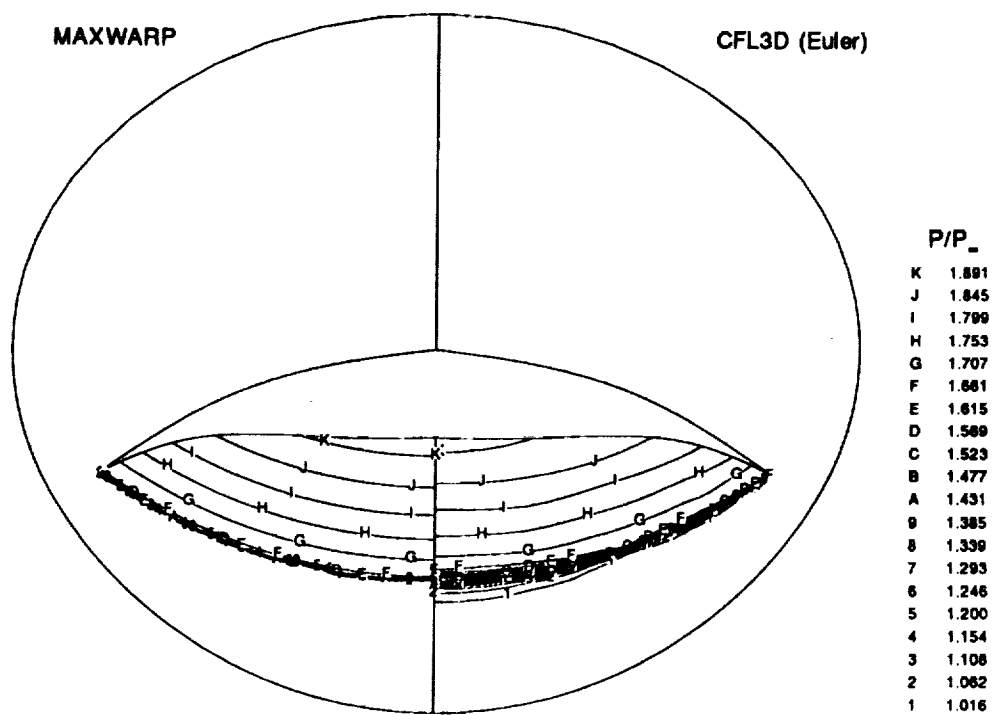


Figure 6.3: Comparison of MAXWARP results and CFL3D Euler results for Mach 6 calculation: Pressure contour at exit flow plane.

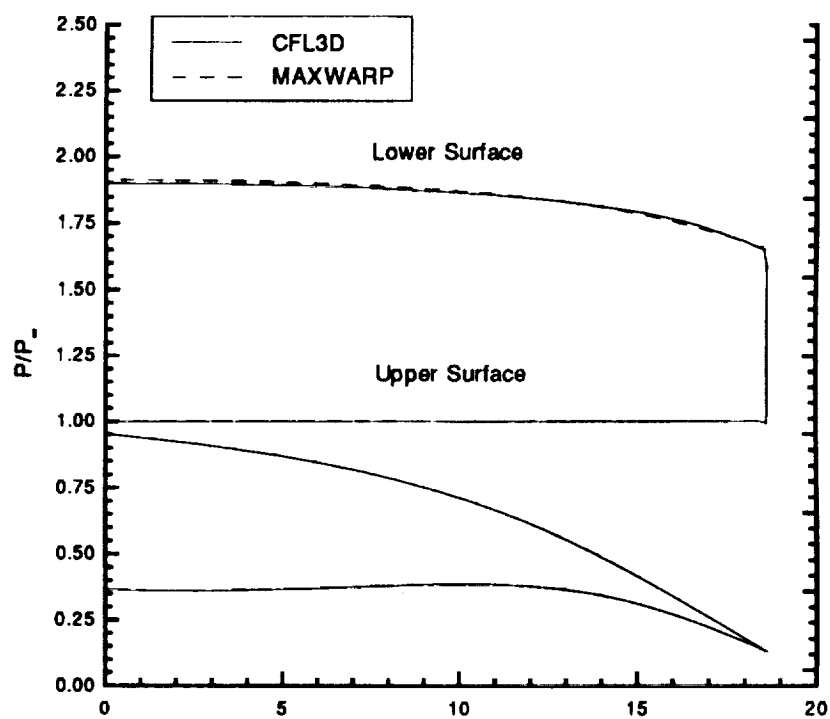


Figure 6.4: Comparison of MAXWARP results and CFL3D Euler results for Mach 6 calculation: Surface pressure distribution at exit flow plane and the outline of the cross-section.

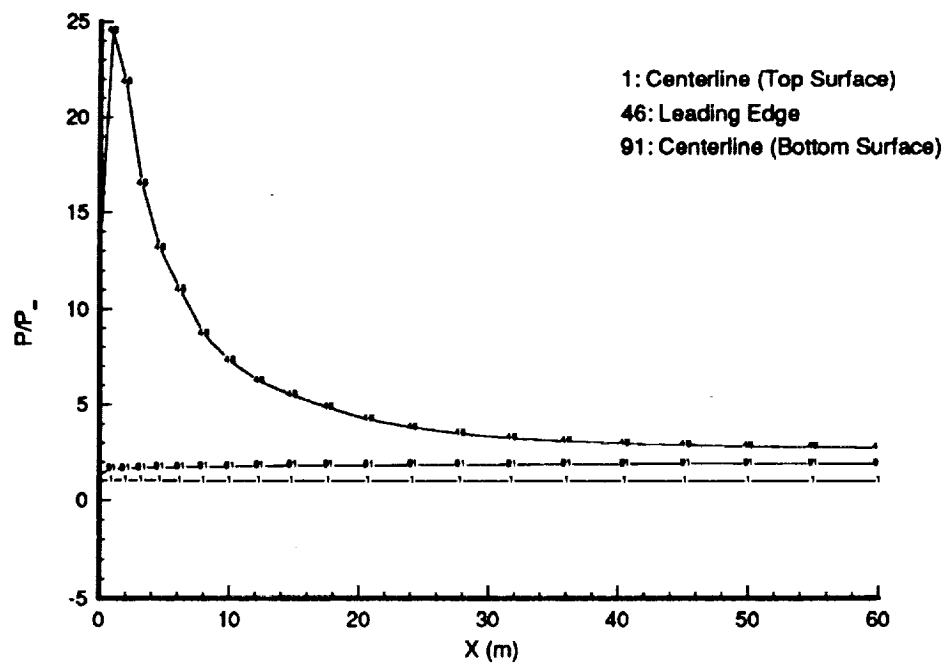


Figure 6.5: Surface pressure variation in the streamwise direction from CFL3D results for Mach 6 calculation

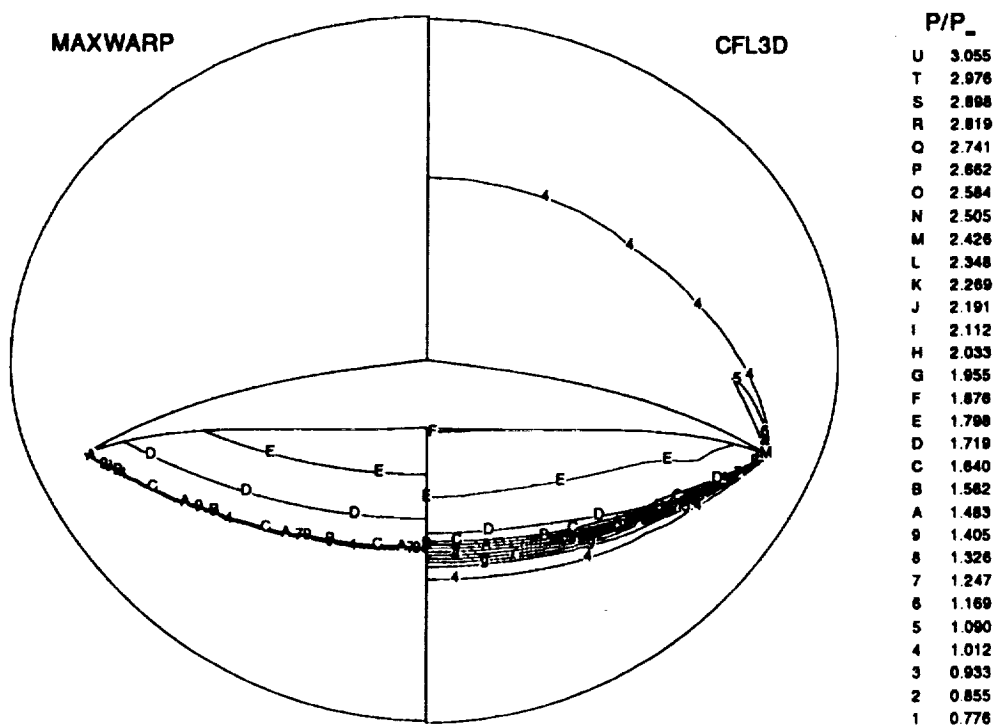


Figure 6.6: Comparison of MAXWARP results and CFL3D results for Mach 6 calculation: Pressure contour at cross-section located at 60 % of the chord.

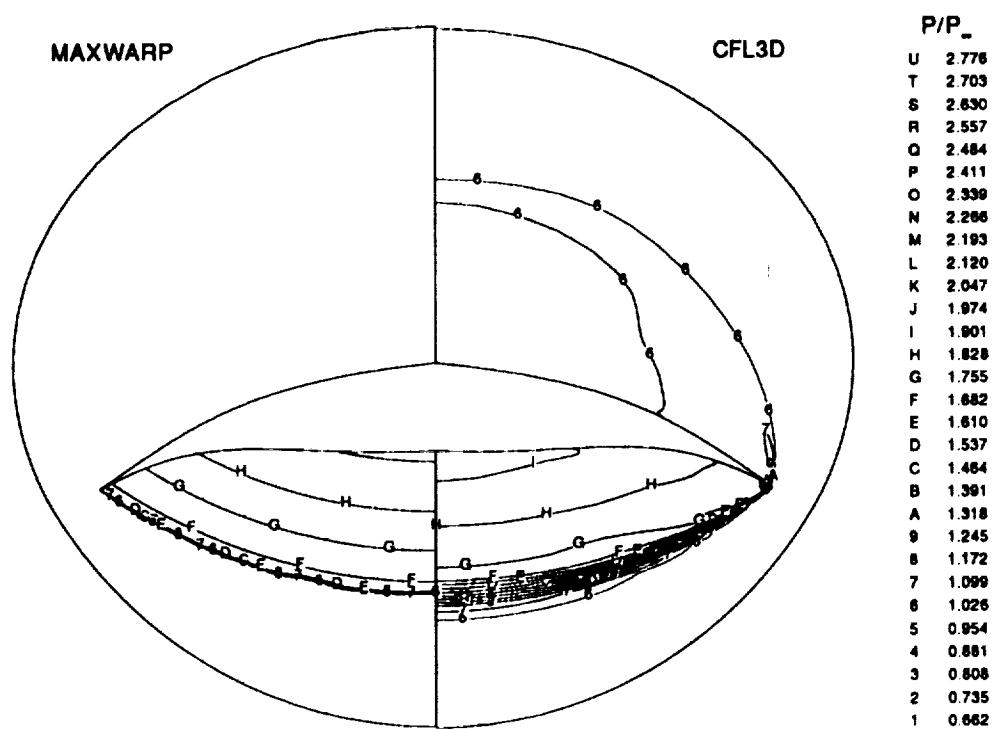


Figure 6.7: Comparison of MAXWARP Results and CFL3D Results for Mach 6 calculation: Pressure contour at exit flow plane.

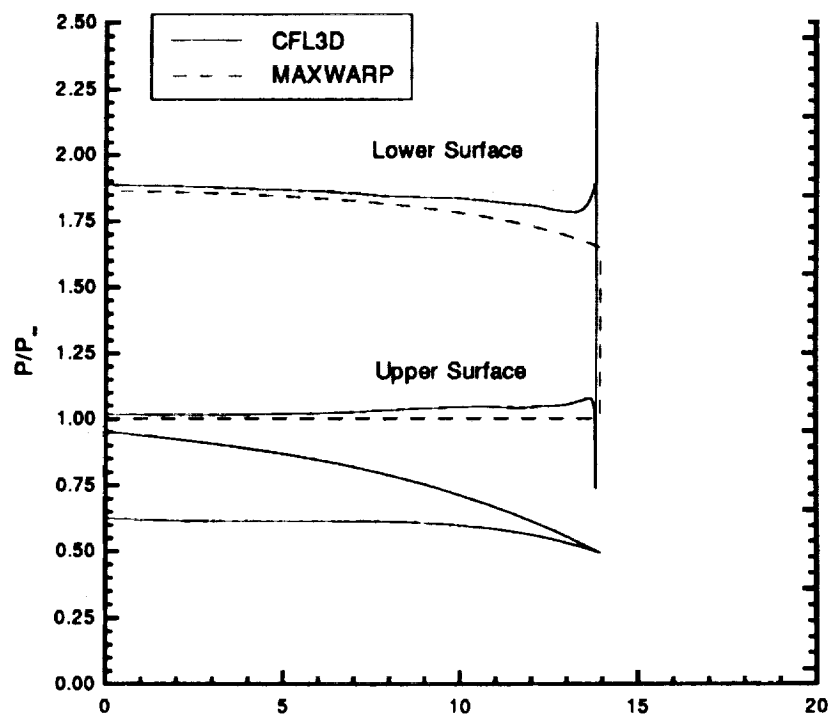


Figure 6.8: Comparison of MAXWARP results and CFL3D results for Mach 6 calculation: Surface pressure distribution at cross-section located at 60 % of the chord and the outline of the cross-section.

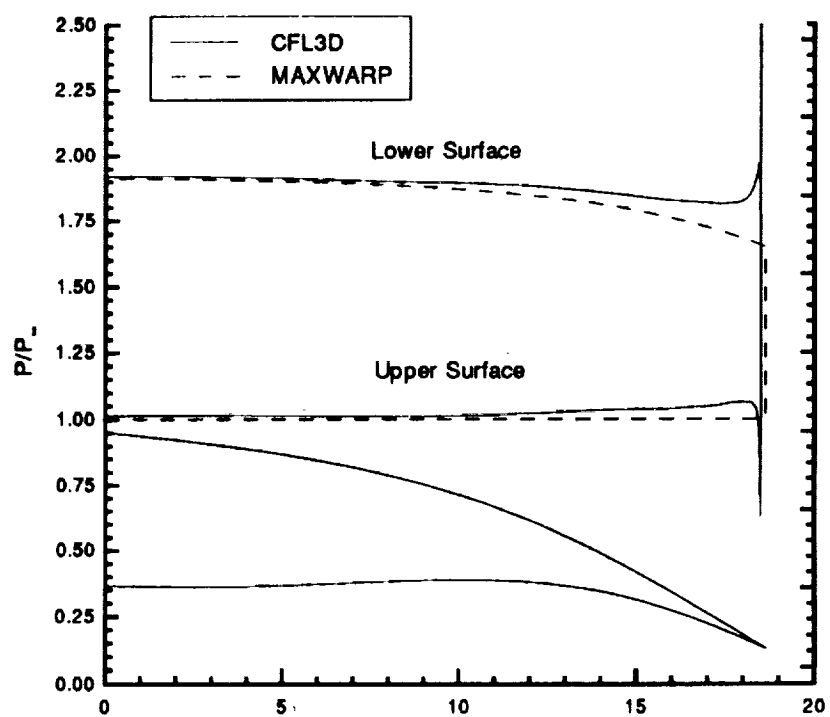


Figure 6.9: Comparison of MAXWARP results and CFL3D results for Mach 6 calculation: Surface pressure distribution at the exit flow plane and the outline of the cross-section.

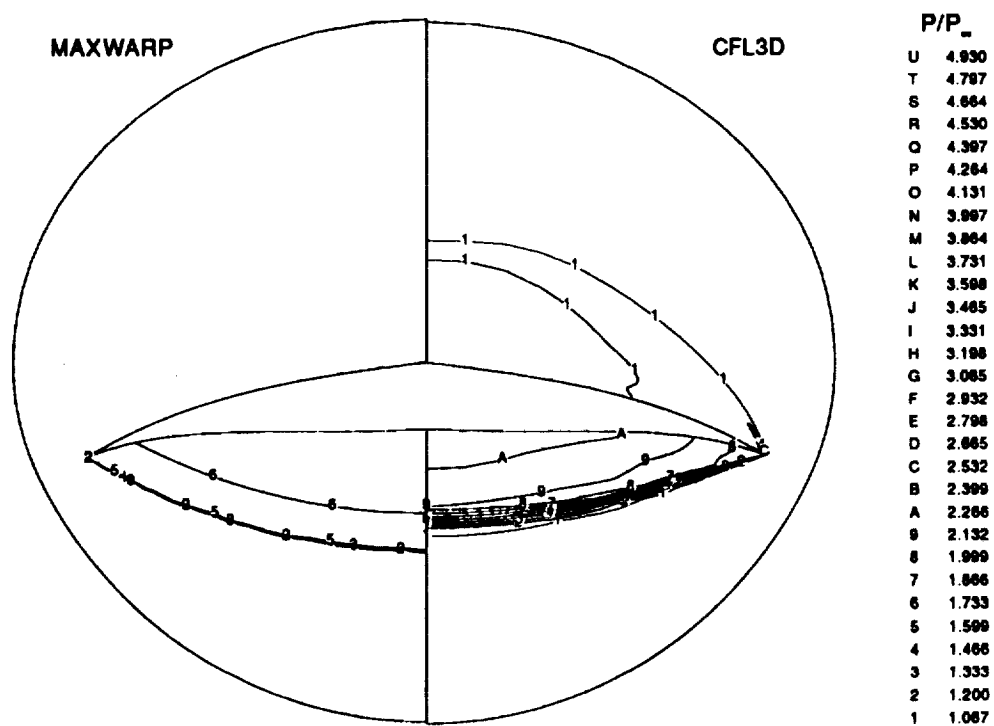


Figure 6.10: Comparison of MAXWARP results for Mach 6 and CFL3D results for Mach 8 calculation: Pressure contour at cross-section located at 60 % of the chord.

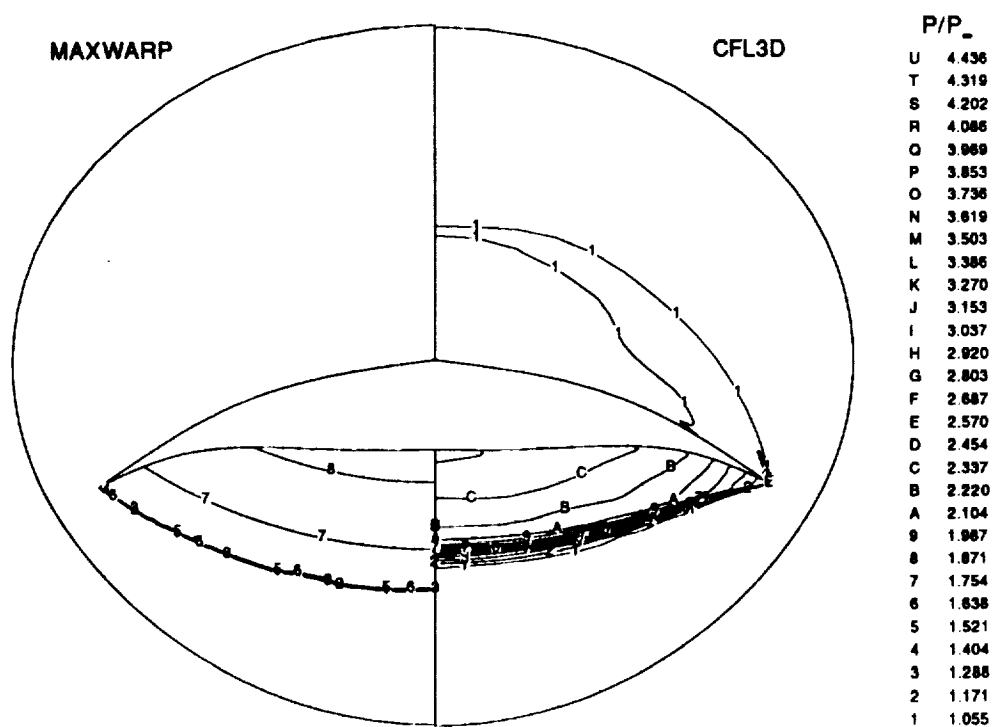


Figure 6.11: Comparison of MAXWARP results for Mach 6 and CFL3D results for Mach 8 calculation: Pressure contour at exit flow plane.

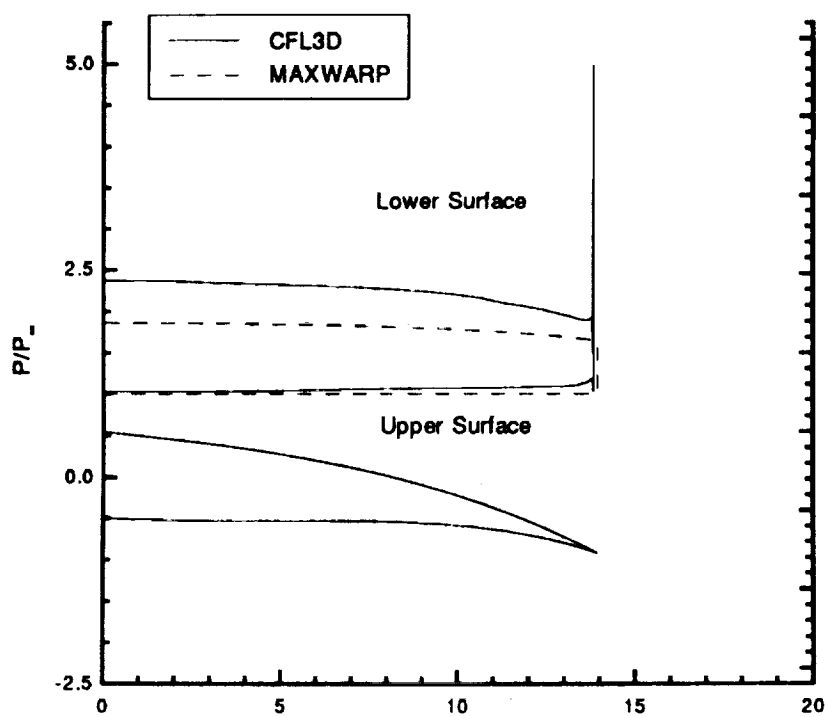


Figure 6.12: Comparison of MAXWARP results for Mach 6 and CFL3D results for Mach 8 calculation: Surface pressure distribution at cross-section located at 60 % of the chord and the outline of the cross-section.

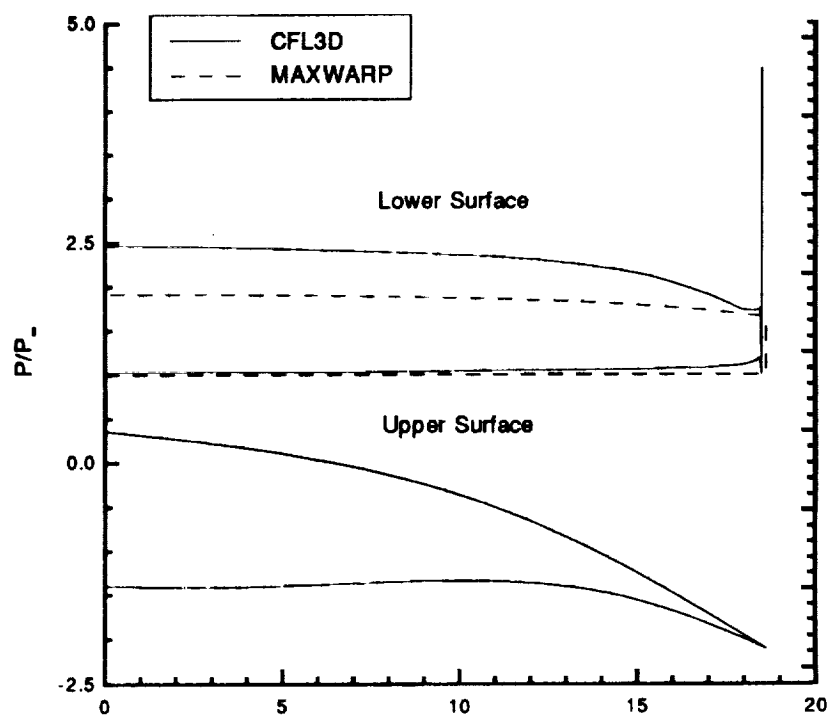


Figure 6.13: Comparison of MAXWARP results for Mach 6 and CFL3D results for Mach 8 calculation: Surface pressure distribution at the exit flow plane and the outline of the cross-section.

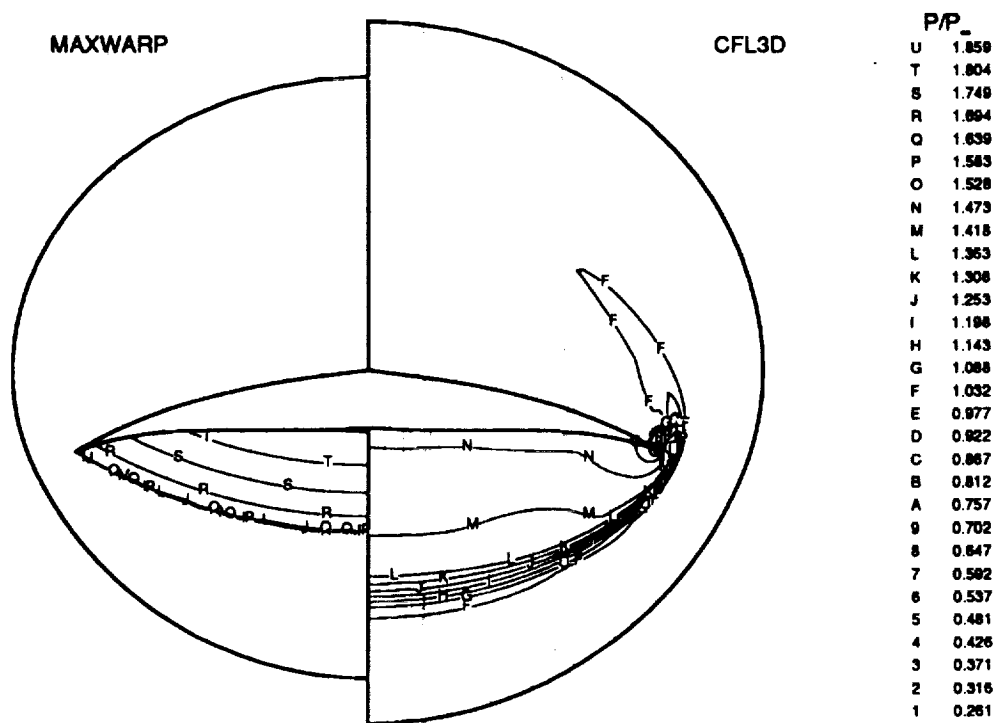


Figure 6.14: Comparison of MAXWARP for Mach 6 results and CFL3D results for Mach 4 calculation: Pressure contour at cross-section located at 60 % of the chord.

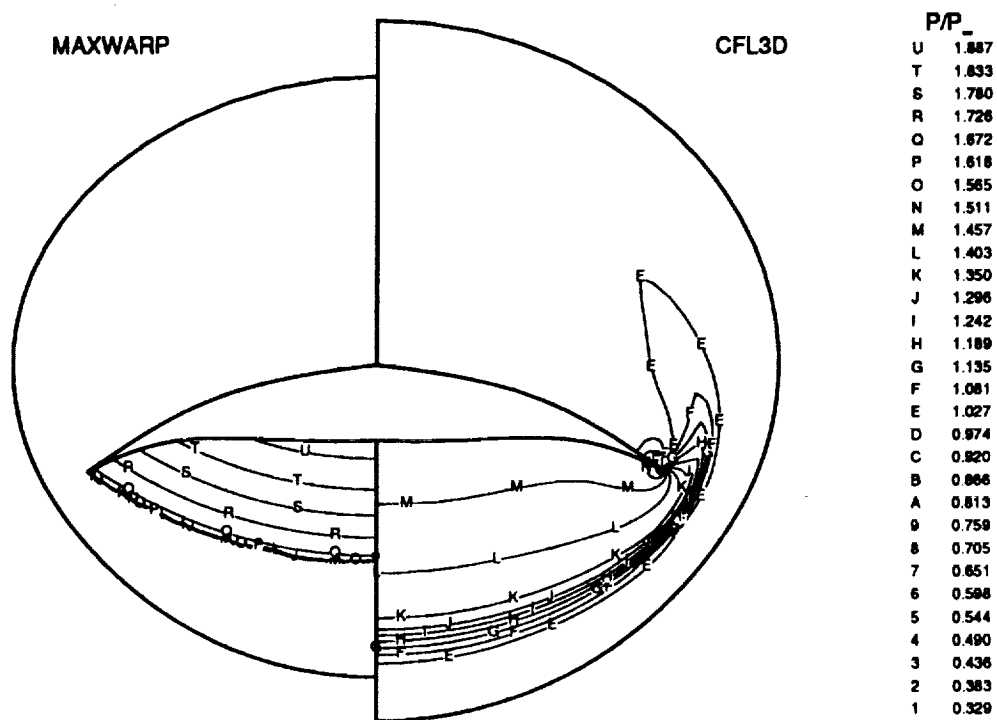


Figure 6.15: Comparison of MAXWARP results for Mach 6 and CFL3D results for Mach 4 calculation: Pressure contour at exit flow plane.

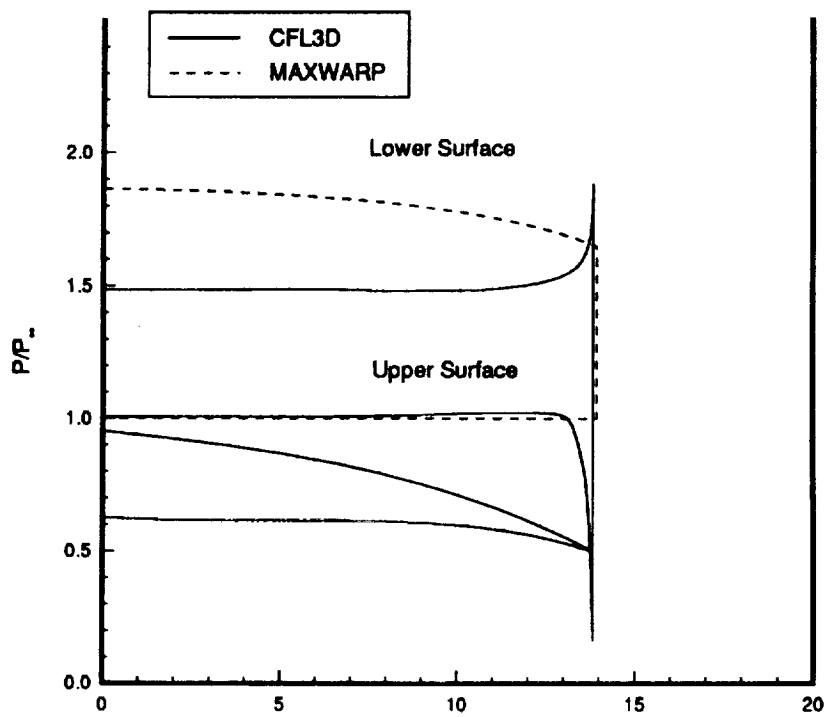


Figure 6.16: Comparison of MAXWARP results for Mach 6 and CFL3D results for Mach 4 calculation: Surface pressure distribution at cross-section located at 60 % of the chord and the outline of the cross-section.

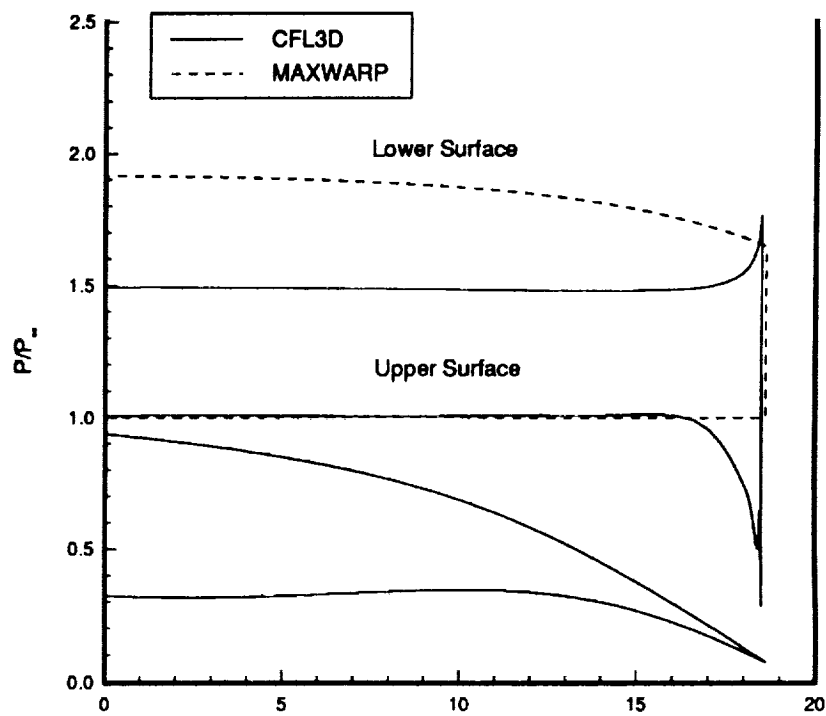


Figure 6.17: Comparison of MAXWARP results for Mach 6 and CFL3D results for Mach 4 calculation: Surface pressure distribution at the exit flow plane and the outline of the cross-section.

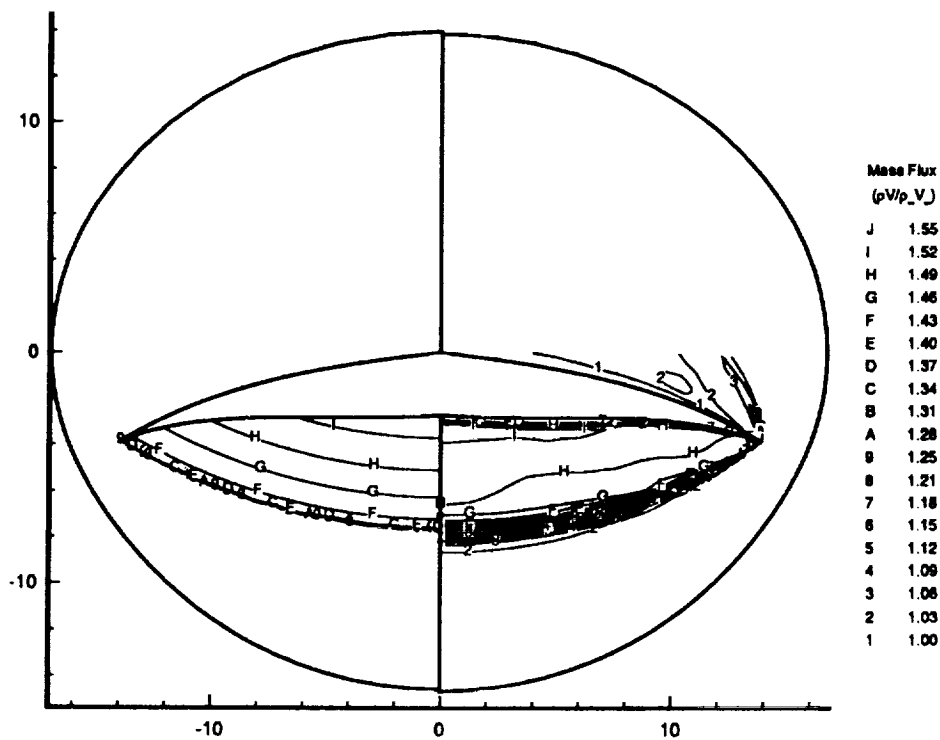


Figure 6.18: Comparison of MAXWARP results and CFL3D results for Mach 6 calculation: Mass flux contour at cross-section located at 60 % of the chord and the outline of the cross-section.

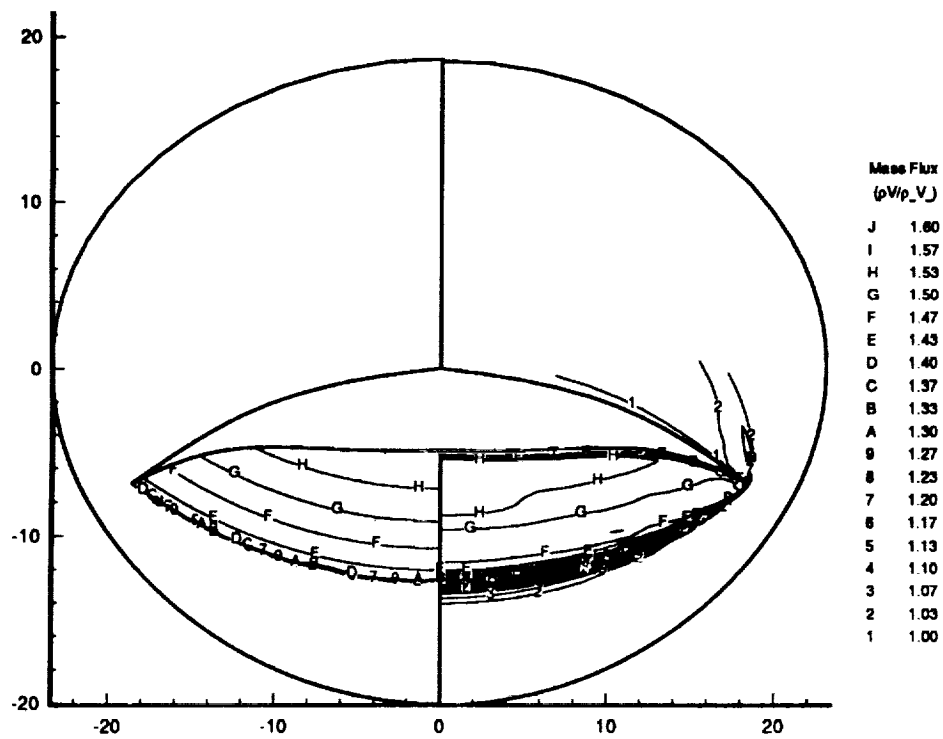


Figure 6.19: Comparison of MAXWARP results and CFL3D results for Mach 6 calculation: Mass flux contour at the exit flow plane and the outline of the cross-section.

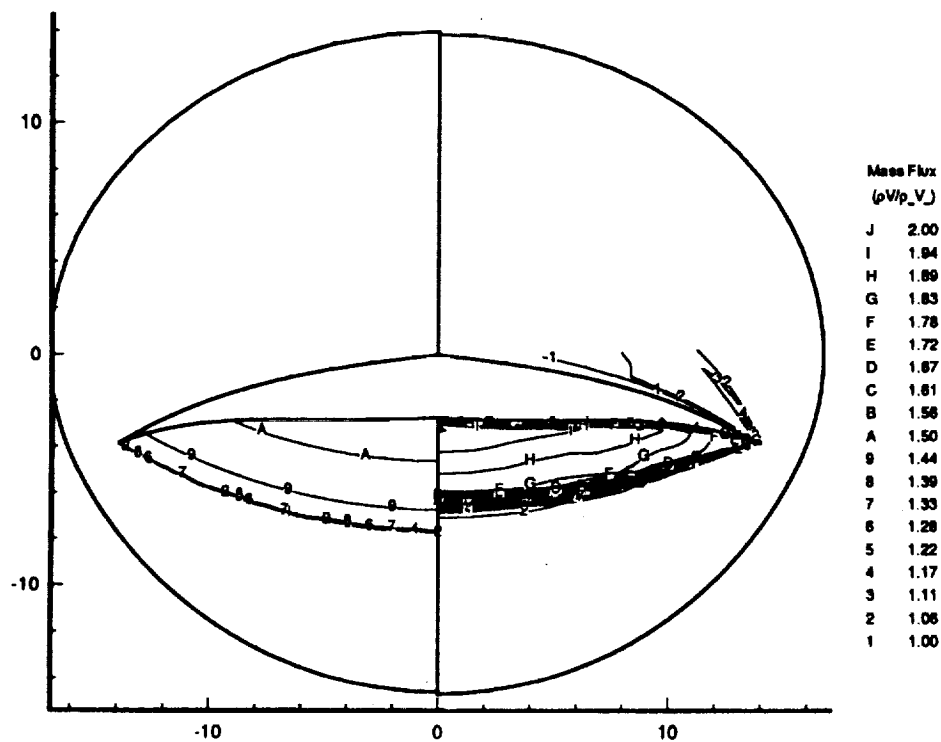


Figure 6.20: Comparison of MAXWARP results for Mach 6 and CFL3D results for Mach 8 calculation: Mass flux contour at cross-section located at 60 % of the chord and the outline of the cross-section.

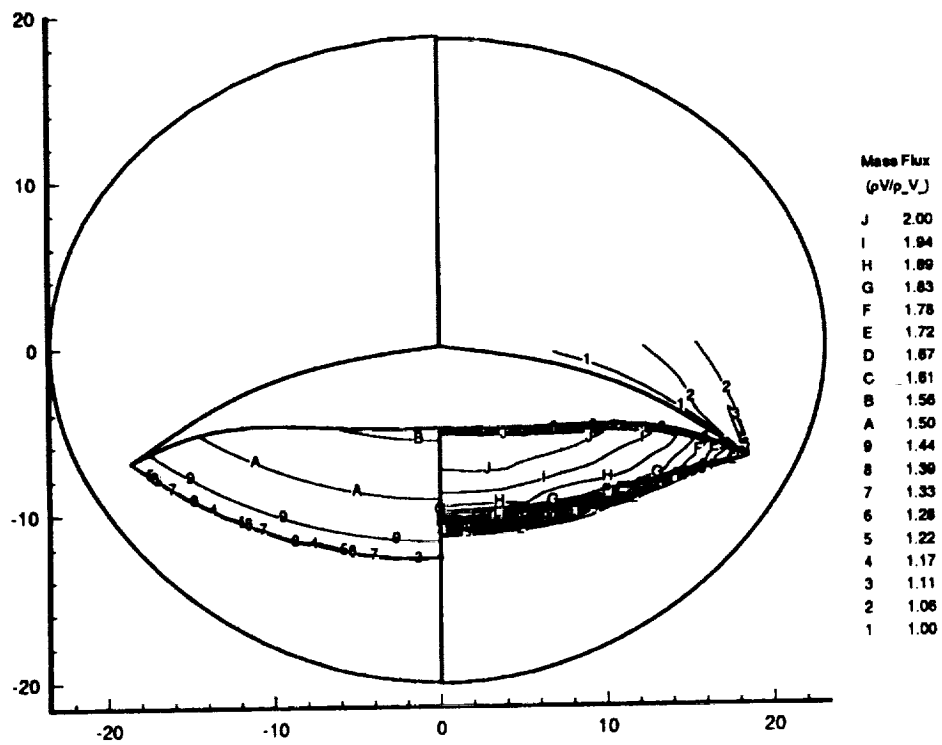


Figure 6.21: Comparison of MAXWARP results for Mach 6 and CFL3D results for Mach 8 calculation: Mass flux contour at the exit flow plane and the outline of the cross-section.

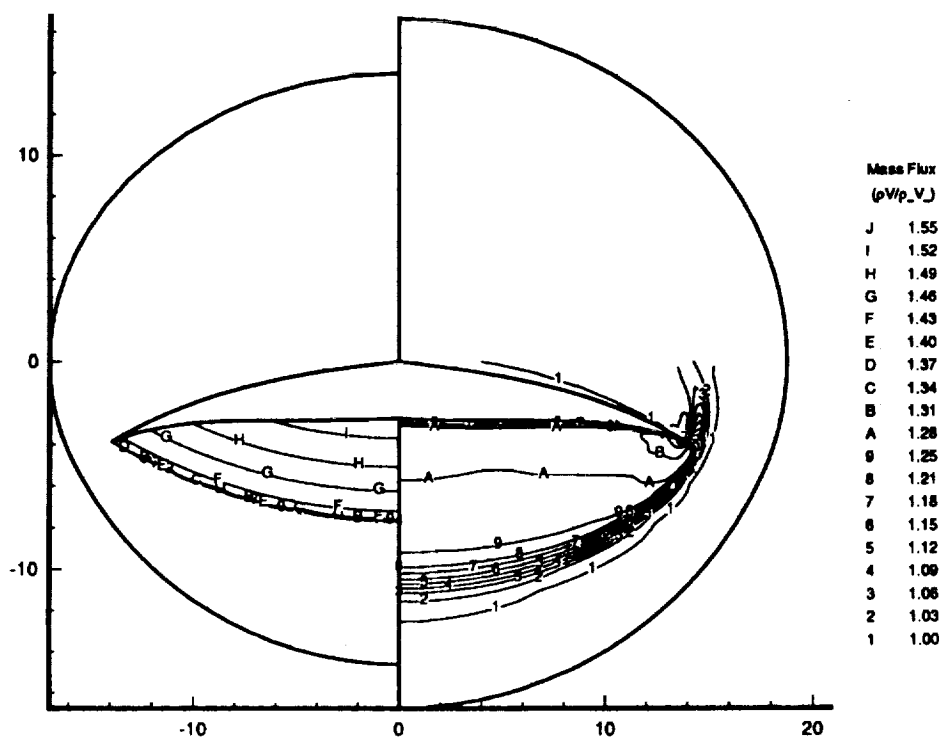


Figure 6.22: Comparison of MAXWARP results for Mach 6 and CFL3D results for Mach 4 calculation: Mass flux contour at cross-section located at 60 % of the chord and the outline of the cross-section.

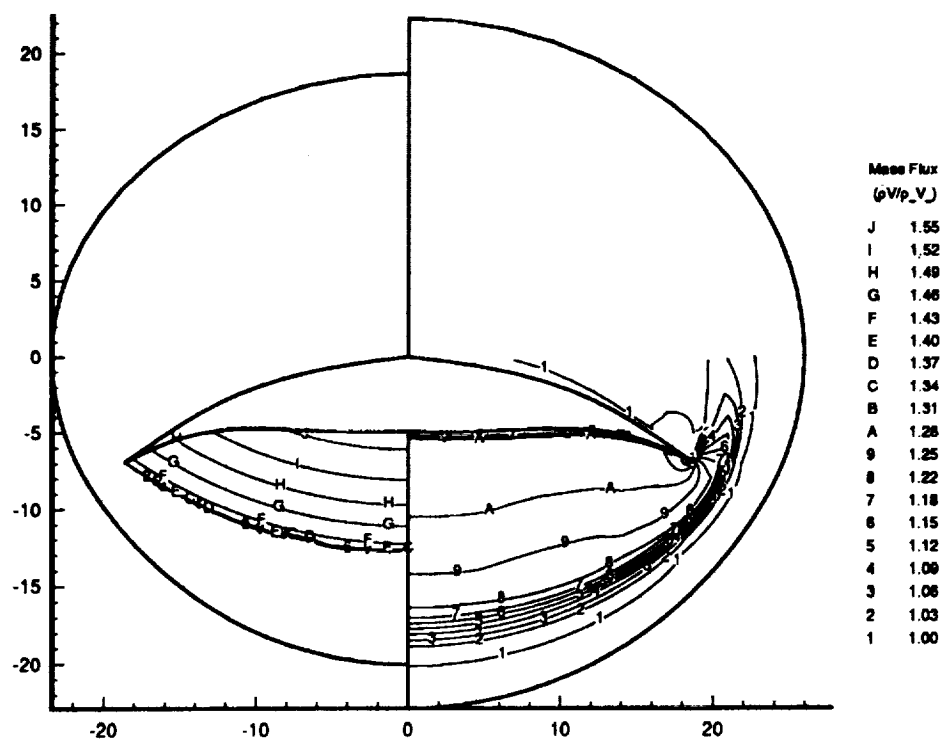


Figure 6.23: Comparison of MAXWARP results for Mach 6 and CFL3D results for Mach 4 calculation: Mass flux contour at the exit flow plane and the outline of the cross-section.

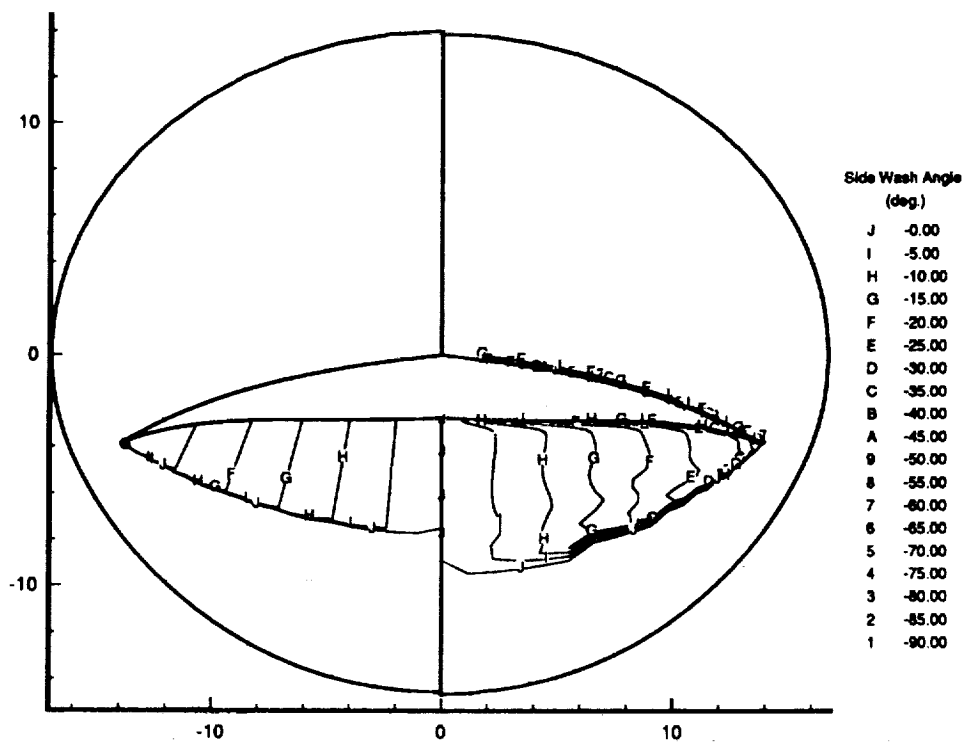


Figure 6.24: Comparison of MAXWARP results and CFL3D results for Mach 6 calculation: Side wash angle contour at cross-section located at 60 % of the chord and the outline of the cross-section.

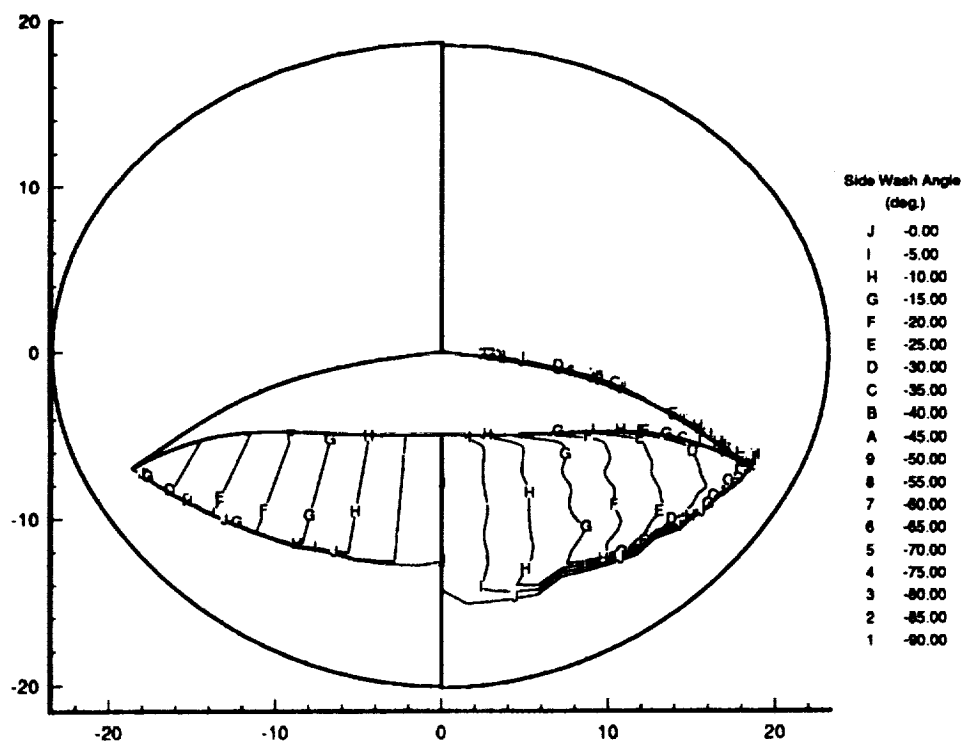


Figure 6.25: Comparison of MAXWARP results and CFL3D results for Mach 6 calculation: Side wash angle contour at the exit flow plane and the outline of the cross-section.

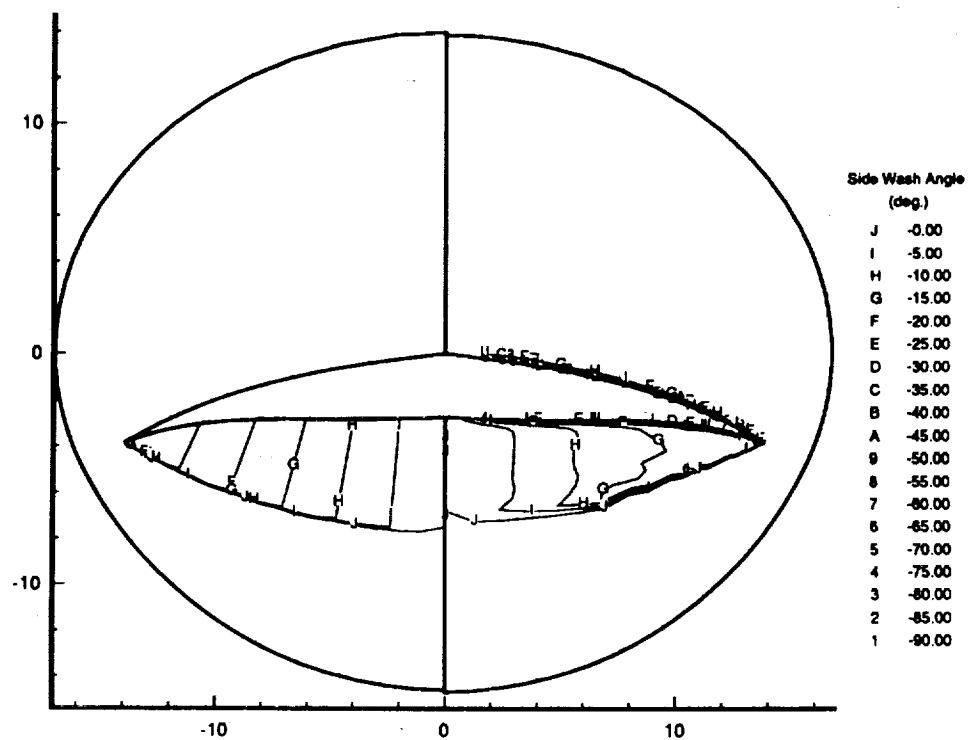


Figure 6.26: Comparison of MAXWARP results for Mach 6 and CFL3D results for Mach 8 calculation: Side wash angle contour at cross-section located at 60 % of the chord and the outline of the cross-section.

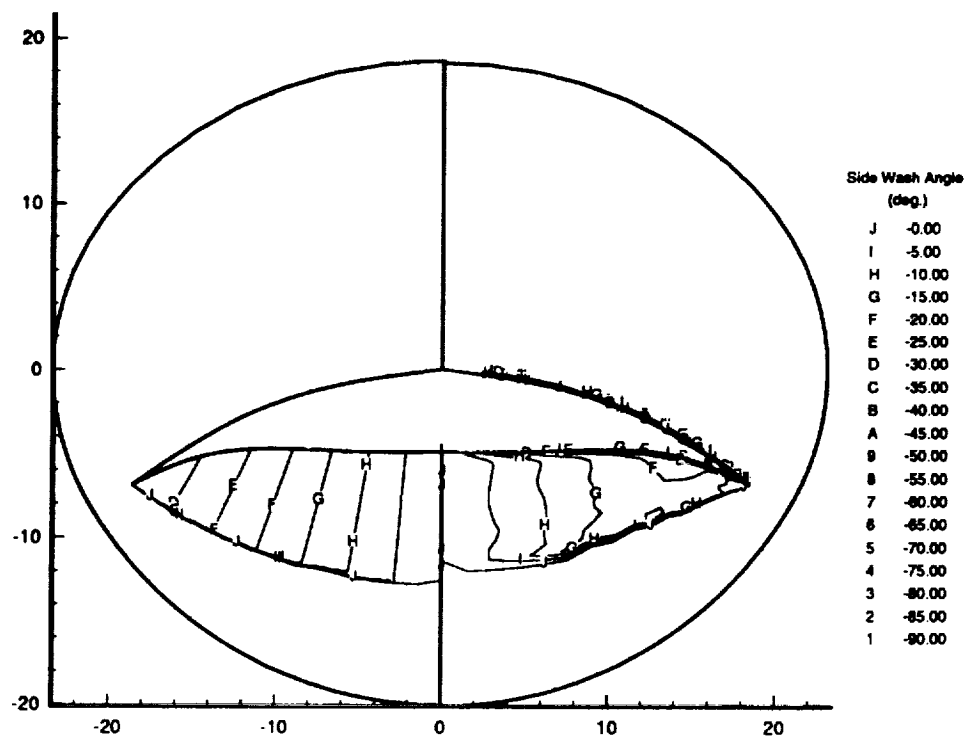


Figure 6.27: Comparison of MAXWARP results for Mach 6 and CFL3D results for Mach 8 calculation: Side wash angle contour at the exit flow plane and the outline of the cross-section.

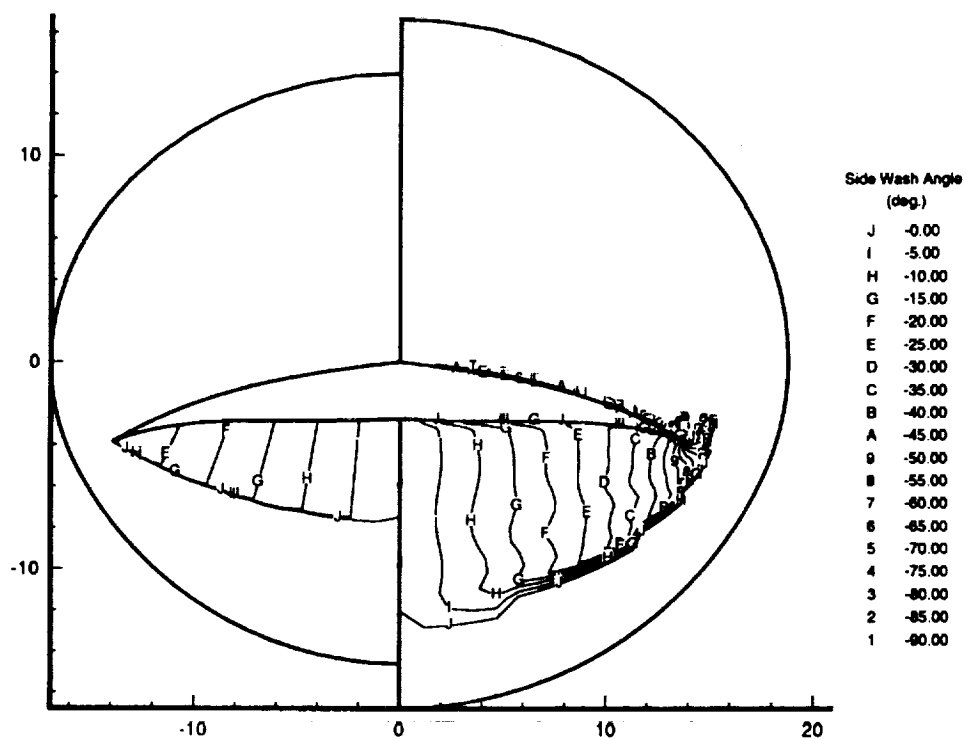


Figure 6.28: Comparison of MAXWARP results for Mach 6 and CFL3D results for Mach 4 calculation: Side wash angle contour at cross-section located at 60 % of the chord and the outline of the cross-section.

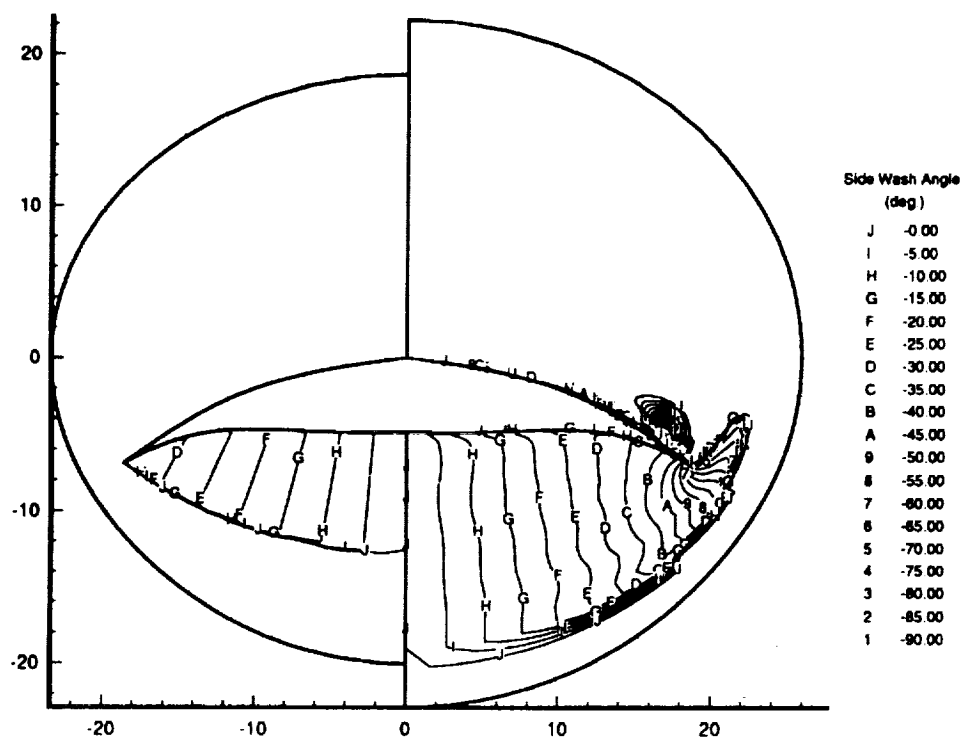


Figure 6.29: Comparison of MAXWARP results for Mach 6 and CFL3D results for Mach 4 calculation: side wash angle at the exit flow plane and the outline of the cross-section.

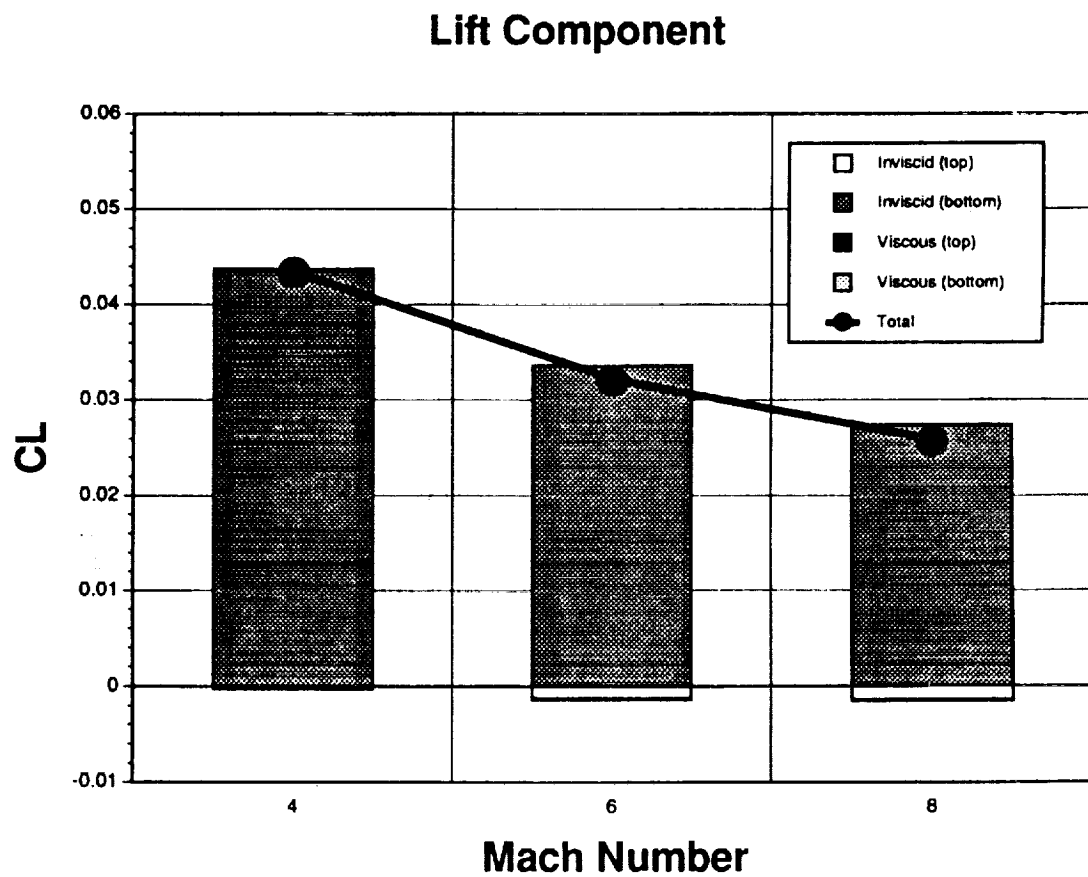


Figure 6.30: Inviscid and viscous force contribution to the total lift coefficient.

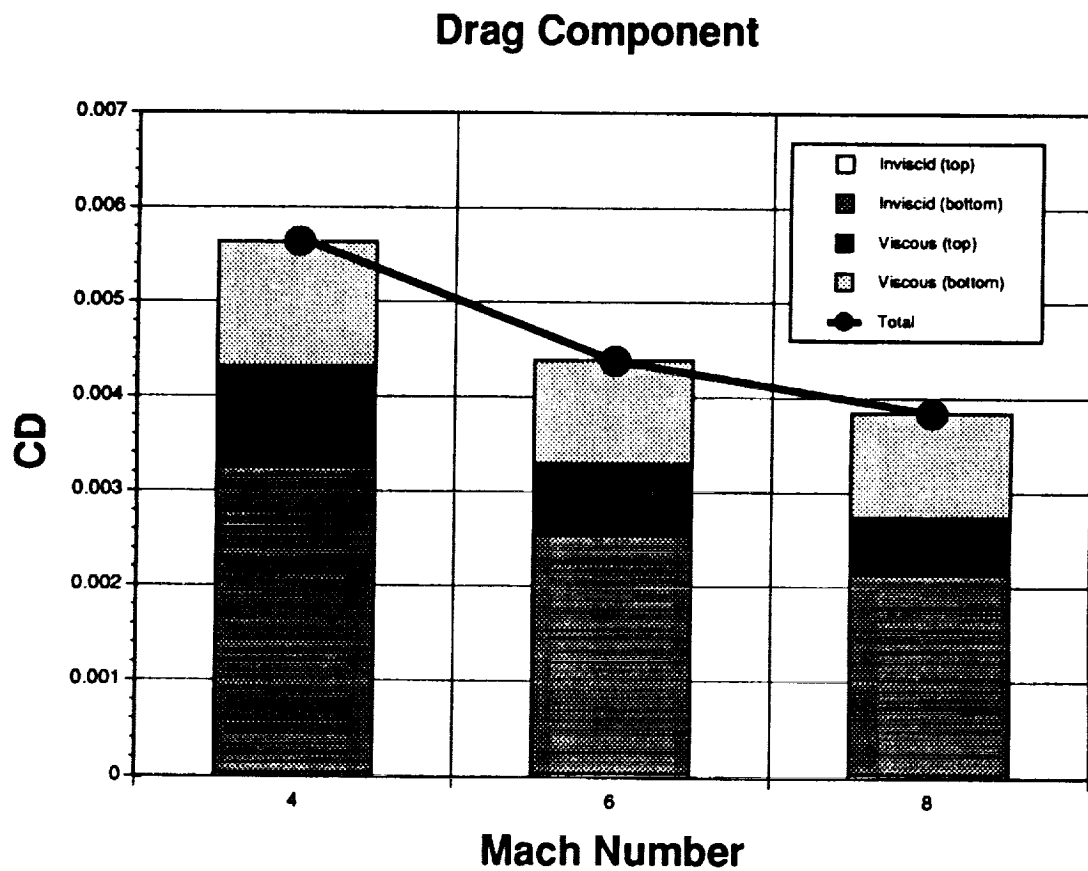


Figure 6.31: Inviscid and viscous force contribution to the total drag coefficient.

L/D of Waveriders

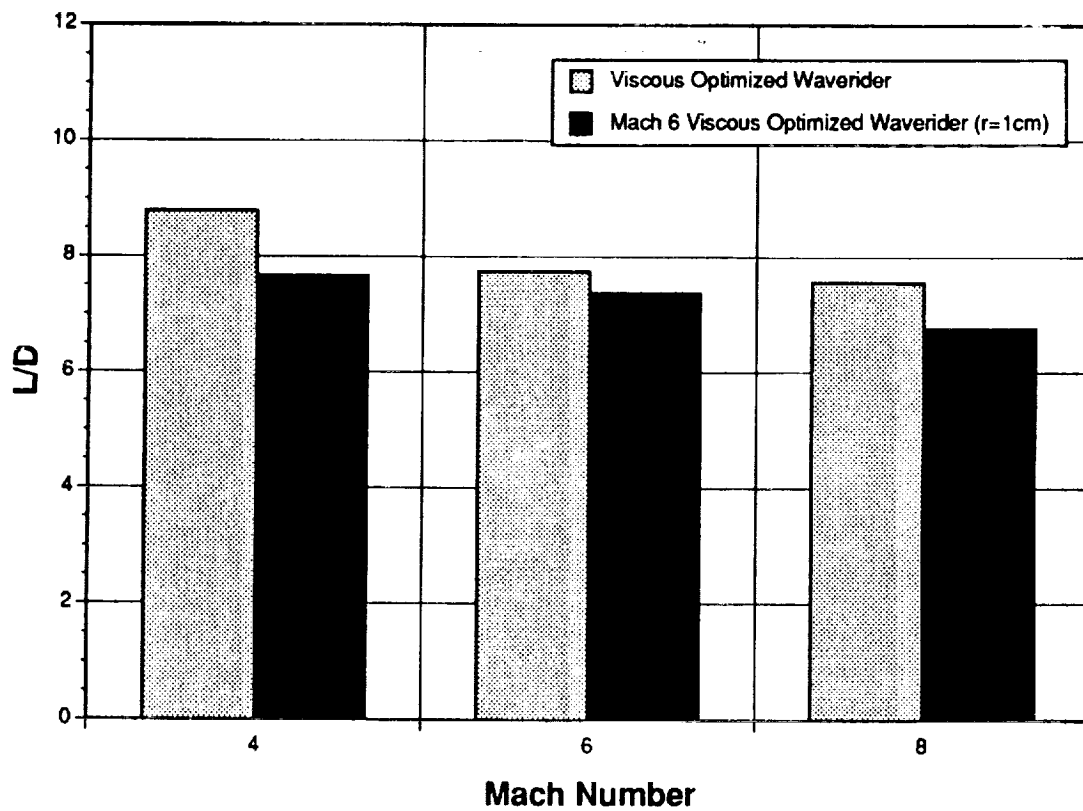


Figure 6.32: Comparison between the L/D values calculated by CFL3D for the Mach 6 viscous optimized waverider and the L/D values predicted by MAXWARP for the Mach 4, 6, and 8 viscous optimized waveriders.

Chapter 7

Conclusions and Recommendations

7.1 Conclusions

The present work is the first Navier-Stokes computation of the viscous optimized waverider at off-design Mach numbers. Navier-Stokes calculations were made at Mach numbers 4, 6, and 8 for a Mach 6 viscous optimized waverider. Good comparisons were found between the inviscid forces from MAXWARP and the Euler solution from CFL3D; thus, validating the inviscid solver of CFL3D. Good comparison also resulted between MAXWARP and the Navier-Stokes calculations at the on-design condition. Especially, excellent agreement was obtained between the two codes for the contribution of viscous effects on drag. From these results, it can be stated that MAXWARP can be used with confidence for preliminary design of hypersonic forebodies. From the Mach 6 calculation it was observed that the rounding of the leading edge to 0.01 m radius had a negligible effect on the containment and the structure of the inviscid flowfield on the lower surface as well as the overall performance of the vehicle; however, some effects were noted in the side wash angle distribution in the boundary layer. Computational results for the off-design Mach numbers demonstrate that the performance of the optimized waverider does not degenerate rapidly with off-design conditions as initially feared, and in actuality the

performance at off-design conditions compares well with the performance of waveriders optimized for those conditions. The uniformity of key flow parameters for inlet performance was maintained throughout the range of Mach numbers which demonstrates that the configuration will make an excellent forebody design for a hypersonic cruise vehicle.

7.2 Recommendations

Because the primary objective of this numerical experiment was to obtain force data for the Mach 6 waverider for on and off design conditions, no detail analysis of the flow within the boundary layer was done. The thickness of the boundary layer at the end of the forebody can have significant effect on the combustor performance. The boundary layer thickness based on velocity profile for the Mach 6 case was approximately 40.0 cm at the exit flow plane, which is consistent with the presently available correlation for the turbulent boundary layer thickness. If this value is indeed correct, then some method to reduce the boundary layer thickness will be necessary. Thus it is important for the future development of the engine/airframe integrated design to do a detailed analysis of the boundary layer at high Reynolds number.

Calculations should be done for different waverider shapes to see whether some sacrifice in performance at the on-design condition can improve the off-design performance.

Finally, as the design matures for the air-breathing hypersonic vehicle, calculations should be performed at multiple points along the flight path for the entire vehicle.

Appendix A

Leading Edge Coordinates

Y	Z
0.00000E+00	1.98334E+01
3.72455E-01	1.98769E+01
7.44910E-01	1.99210E+01
1.11737E+00	1.99659E+01
1.48982E+00	2.00119E+01
1.86228E+00	2.00590E+01
2.23473E+00	2.01077E+01
2.60719E+00	2.01580E+01
2.97964E+00	2.02102E+01
3.35210E+00	2.02645E+01
3.72455E+00	2.03212E+01
4.09701E+00	2.03804E+01
4.46946E+00	2.04424E+01
4.84192E+00	2.05074E+01
5.21437E+00	2.05756E+01
5.58683E+00	2.06472E+01
5.95928E+00	2.07225E+01
6.33174E+00	2.08016E+01
6.70419E+00	2.08849E+01
7.07665E+00	2.09725E+01
7.44910E+00	2.10648E+01
7.82156E+00	2.11620E+01
8.19401E+00	2.12645E+01
8.56647E+00	2.13723E+01
8.93892E+00	2.14860E+01
9.31138E+00	2.16056E+01

Table A.1: Leading edge coordinates for Mach 6 viscous optimized waverider.

Y	Z
9.68384E+00	2.17315E+01
1.00563E+01	2.18640E+01
1.04287E+01	2.20033E+01
1.08012E+01	2.21498E+01
1.11737E+01	2.23036E+01
1.15461E+01	2.24650E+01
1.19186E+01	2.26344E+01
1.22910E+01	2.28119E+01
1.26635E+01	2.29979E+01
1.30359E+01	2.31920E+01
1.34084E+01	2.33939E+01
1.37808E+01	2.36030E+01
1.41533E+01	2.38187E+01
1.45258E+01	2.40406E+01
1.48982E+01	2.42681E+01
1.52707E+01	2.45008E+01
1.56431E+01	2.47381E+01
1.60156E+01	2.49795E+01
1.63880E+01	2.52245E+01
1.67605E+01	2.54725E+01
1.71329E+01	2.57232E+01
1.75054E+01	2.59759E+01
1.78779E+01	2.62301E+01
1.82503E+01	2.64853E+01
1.86228E+01	2.67411E+01

Table A.2: Leading edge coordinates for Mach 6 viscous optimized waverider. (continued)

Bibliography

- ¹ United States General Accounting Office Report to Congressional Committees, "National Aero-Space Plane, A Technology Development and Demonstration Program to Build the X-30," GAO/NSIAD-88-122, April 1988.
- ² Edwards, C. L. W., Small, W. J. , Weinder, J. P., and Johnston, P. J., "Studies of Scramjet/Airframe Integration Techniques for Hypersonic Aircraft," AIAA-75-0058, Jan. 1975.
- ³ Nonweiler, T. R. F., "Aerodynamic Problems of Manned Space Vehicles," *Journal of the Royal Aeronautical Society*, Vol. 63, 1959, pp. 521-528.
- ⁴ Bowcutt, K. G. and Anderson, J. D., Jr., "Viscous Optimized Waveriders," AIAA-87-0272, Jan. 1987.
- ⁵ Vanhoy, D., *Low-Speed Wind Tunnel Testing of a Mach 6 Viscous Optimized Waverider*, Master of Science Thesis, Department of Aerospace Engineering, University of Maryland, College Park, Maryland, 1988.
- ⁶ Bauer, S. X., Covell, P.F., Forrest, D.K., and McGrath, B.E., "Preliminary Assessment of a Mach 4 and Mach 6 Waverider," First International Hypersonic Waverider Symposium, University of Maryland, College Park, Maryland, October 17-19, 1990.
- ⁷ O'Neill, M. K., and Lewis, M. J., "Optimized Scramjet Integration on a Waverider," AIAA Paper 91-1693, June 1991.
- ⁸ Rasmussen, M. L., "Waverider Configurations Derived from Inclined Circular and Elliptic Cones," *Journal of the Royal Spacecraft and Rockets*, Vol. 17, No. 6, Nov.-Dec. 1980, pp. 537-545.
- ⁹ Rasmussen, M. L. and Clement, L. W., "Cone-Derived Waveriders with Longitudinal Curvature," AIAA Paper 84-2100, 1984.

- ¹⁰ Cole, J. D. and Zien, T. F., "A Class of Three-Dimensional Optimum Hypersonic Wings," *AIAA Journal*, Vol. 7., No. 2, Feb. 1969, pp. 264-271.
- ¹¹ Kim, B. S., Rasmussen, M. L., and Jischke, M. C. , "Optimization of Waverider Configuration Generated from Axisymmetric Conical Flows," AIAA Paper 82-1299, 1982.
- ¹² Sobieczky, H., Dougherty, F. C., and Jones, K. D., "Hypersonic Waverider Design from Given Shock Waves," First International Hypersonic Waverider Symposium, University of Maryland, College Park, Maryland, October 17-19, 1990.
- ¹³ Nelder, J. A., Mead, R., "A Simplex Method for Function Minimization", *Computer Journal*, Vol. 7., Jan. 1965, pp. 308-313.
- ¹⁴ Kuchemann, D., *The Aerodynamic Design of Aircraft*, Pergamon Press, Oxford, 1978, pp. 448-510.
- ¹⁵ Corda, S. and Anderson, J. D., Jr., "Viscous Optimized Hypersonic Waveriders Designed from Axisymmetric Flow Fields," AIAA 88-0369, Jan. 1988.
- ¹⁶ McLaughlin, T. A., *Viscous Optimized Hypersonic Waveriders for Chemical Equilibrium Flow*, Master of Science Thesis, Department of Aerospace Engineering, University of Maryland, College Park, Maryland, 1990.
- ¹⁷ Vanmol, D., *Heat Transfer Characteristics of Hypersonic Waveriders with Emphasis on the Leading Edge Effects*, Master of Science Thesis, Department of Aerospace Engineering, University of Maryland, College Park, Maryland, 1991.
- ¹⁸ Anderson, J. D., Jr., McLaughlin, T. A., Chang, J., "Hypersonic Waveriders: Effects of Chemically Reacting Flow and Viscous Interaction," AIAA 92-0302, Jan. 1992.
- ¹⁹ Baldwin, B. S., and Lomax, H., "Thin Layer Approximation and Algebraic Model for Separated Turbulent Flows," AIAA Paper 78-257, 1978.
- ²⁰ Vasta, V. N., Thomas, J. L., and Wedan, B. W., "Navier-Stokes Computations of Prolate Spheroids at Angle of Attack," AIAA Paper 87-2627, 1987.
- ²¹ Thomas, J. L., Taylor, S. L., and Anderson, W.K., "Navier-Stokes Computation of Vortical Flows Over Low Aspect Ratio Wings," AIAA Paper 87-0207, 1987.

- ²² Roe, P. L., "Characteristic Based Schemes for the Euler Equations," *Annual Review of Fluid Mechanics*, 1986, pp. 377-365.
- ²³ Godunov, S. K., "A Difference Scheme for Numerical Computaion of Discontinuous Solution of Hydrodynamic Equations," *Math. Sbornik*, Vol. 47, 1959, pp. 357-393.
- ²⁴ Coakley, T. L., "Implicit Methods for Compressible Navier-Stokes Equations," AIAA Paper 87-1107-CP, 1987.
- ²⁵ Steger, J. L., and Sorenson, R. L., "Automatic Mesh-Point Clustering Near a Boundary in Grid Generation with Elliptic Partial Differential Equations," *Journal of Computational Physics*, Vol. 33, 1979, pp. 405-410.
- ²⁶ Hsu, A. and Lytle, J., "A Simple Algebraic Grid Adaptation Scheme with Applications to Two- and Three-Dimensional Flow Problems," AIAA Paper 89-1984-CP, 1989.

REPORT DOCUMENTATION PAGE			Form Approved OMB No. 0704-0188	
<small>Public reporting burden for this collection of information is estimated to average 1 hour per response, including the time for reviewing instructions, searching existing data sources, gathering and maintaining the data needed, and completing and reviewing the collection of information. Send comments regarding this burden estimate or any other aspect of this collection of information, including suggestions for reducing this burden, to Washington Headquarters Services, Directorate for Information Operations and Reports, 1215 Jefferson Davis Highway, Suite 1204, Arlington, VA 22202-4302, and to the Office of Management and Budget, Paperwork Reduction Project (0704-0188), Washington, DC 20503.</small>				
1. AGENCY USE ONLY (Leave blank)		2. REPORT DATE June 1992		3. REPORT TYPE AND DATES COVERED Contractor Report
4. TITLE AND SUBTITLE Navier-Stokes Computations of a Viscous Optimized Waverider			5. FUNDING NUMBERS G NAG1-1192 WU 505-59-40-10	
6. AUTHOR(S) Naruhisa Takashima				
7. PERFORMING ORGANIZATION NAME(S) AND ADDRESS(ES) University of Maryland Department of Aerospace Engineering College Park, MD 20742			8. PERFORMING ORGANIZATION REPORT NUMBER UM-AERO 92-08	
9. SPONSORING/MONITORING AGENCY NAME(S) AND ADDRESS(ES) National Aeronautics and Space Administration Langley Research Center Hampton, VA 23665-5225			10. SPONSORING/MONITORING AGENCY REPORT NUMBER NASA CR-189658	
11. SUPPLEMENTARY NOTES The information presented in this report was offered as a thesis in partial fulfillment of the requirements for the Degree of Master of Science, University of Maryland, College Park, MD, May 1992. Langley Technical Monitor: Lawrence D. Huebner				
12a. DISTRIBUTION/AVAILABILITY STATEMENT Unclassified - Unlimited Subject Category 02			12b. DISTRIBUTION CODE	
13. ABSTRACT (Maximum 200 words) The performance of a Mach 6 viscous optimized waverider was calculated using the three-dimensional Navier-Stokes equations. The Mach 6 viscous optimized waverider was generated using MAXWARP, a code developed at the University of Maryland. The computations were performed using CFL3D, an implicit upwind-biased finite-volume algorithm developed at NASA Langley. Results show that good agreement was found between the calculated performance by MAXWARP and results from the Mach 6 Navier-Stokes computation. Furthermore, off-design performance of the Mach 6 optimized waverider was computed at Mach 4 and 8. The performance at these Mach numbers compared well with the performance of the viscous optimized waveriders specifically designed for these Mach numbers. Finally, contours of different flow parameters in the cross-flow plane were examined for the three calculations. The results indicate that the flow gradients are relatively small within the captured flow, and the variation itself is well behaved; thus, making the waverider configuration a promising choice for an engine/airframe design, especially for cruise-type applications.				
14. SUBJECT TERMS Viscous Optimized Waveriders Computational Fluid Dynamics			15. NUMBER OF PAGES 101	
Navier-Stokes Equations Aerodynamic Performance Engine/Airframe Integration			16. PRICE CODE A06	
17. SECURITY CLASSIFICATION OF REPORT Unclassified		18. SECURITY CLASSIFICATION OF THIS PAGE Unclassified		19. SECURITY CLASSIFICATION OF ABSTRACT Unclassified
20. LIMITATION OF ABSTRACT				